Multiple sulfur isotopes signature of Thermochemical Sulfate Reduction (TSR): Insights from Alpine Triassic evaporites

Guillaume Barré, Émilie Thomassot, Raymond Michels, Pierre Cartigny, Pierre Strzerzynski, Laurent Truche

Multiple sulfur isotopes signature of Thermochemical Sulfate Reduction (TSR): insights from Alpine Triassic evaporites

Guillaume Barré[1*], Émilie Thomassot[2], Raymond Michels[1], Pierre Cartigny[3], Pierre Strzerzynski[4], Laurent Truche[1,5]

[1]*Université de Lorraine, CNRS, GeoRessources, UMR 7359, BP 70239, F-54506 Vandœuvre-lès-Nancy, France*

[2]*Université de Lorraine, CNRS, UMR 7358, CRPG, Vandœuvre-lès-Nancy, France*

[3]*Université de Paris, Institut de physique du globe de Paris, CNRS, F-75005 Paris, France*

[4]*Laboratoire de Géologie UFR Sciences et Technique, Université du Mans, Avenue O. Messiaen, 72000 Le Mans, France*

[5]*Univ. Grenoble Alpes, Univ. Savoie Mont Blanc, CNRS, IRD, IFSTTAR, ISTerre, 38000 Grenoble, France.*

[*]*e-mail: guillaume.barre.2@ulaval.ca*

**Present address: Département de géologie et génie géologique, centre E4M, Université Laval, Québec, Canada*

Abstract

The sulfur cycle is driven by redox processes, among which sulfate reduction is of primary importance. Sulfate is reduced to sulfide either abiotically by Thermochemical Sulfate Reduction (TSR) or biotically by Microbial Sulfate Reduction (MSR). Although these two processes occur at different temperature regimes (>100°C and <80°C, respectively), they generate similar by-products (e.g., sulfides, elemental sulfur). The $^{34}S/^{32}S$ ratio is often used as the sole criterion to identify the origin of reduced sulfur compounds, but overlaps prevent unambiguous conclusions. Contrary to MSR, the multiple sulfur isotopic signatures ($\delta^{33}S$, $\delta^{34}S$, $\delta^{36}S$) of natural TSR remains uncharacterized. Here, we performed multiple sulfur isotopes

analyses of sulfates, sulfides, and elemental sulfur from six sites in the Alpine Triassic evaporites formation to better constrain the isotopic signatures of TSR. Unlike MSR, TSR can induce slight negative deviations ($\Delta^{33}S$ down to −0.08‰) relative to the initial sulfate $\Delta^{33}S$ value, which significantly discriminates between these two processes. Isotopic equilibria between anhydrite and either elemental sulfur or sulfides (pyrite or chalcopyrite) were verified according to their mass-fractionation exponents ($^{33/34}\theta$ = 0.5140 and 0.5170, respectively). Using sulfate-elemental sulfur ($\Delta^{34}S_{SO_4^{2-}\text{-}S_8}$) or sulfate-sulfide ($\Delta^{34}S_{SO_4^{2-}\text{-}S^{2-}}$) fractionation pairs and respective fractionation factors ($^{34}\alpha$) for samples that fulfilled the criteria of isotopic equilibrium, we determined the precipitation temperatures of elemental sulfur and sulfides (pyrite or chalcopyrite) to be 194 ± 14 °C and 293–488 °C, respectively. Interestingly, the obtained temperature of elemental sulfur precipitation corresponds exactly to the solid-liquid phase transition of native sulfur. Using $\Delta^{33}S$ vs. $\delta^{34}S$ and $\Delta^{33}S$ vs. $\Delta^{36}S$ diagrams, we are able to fully explain the isotopic signatures of disequilibrium sulfides by the mixing of sulfate with either elemental or organic sulfur in the aqueous fluid. Mixing curves allow the determination of the relative proportions of sulfate and organic and elemental sulfur, the latter being formed by the recombination of polysulfides during cooling. It appears that the sulfides' signatures are best explained by a 33% contribution of polysulfides (i.e., elemental sulfur signatures), consistent with the relative proportion of dissolved polysulfides previously measured in fluid inclusions from this formation at >200 °C. Finally, no sulfur mass independent fractionation (S-MIF) is observed in this evaporitic formation, consistent with the TSR signature generated both at equilibrium and by mixing. This implies that TSR does not generate S-MIFs. Our results thus provide multiple sulfur isotopes signatures of TSR, which may be used to reliably identify this process in variable geological settings.

Keywords: Quadrupole sulfur isotopes, TSR, Sulfur cycle, Isotopic equilibrium, Two-components mixing curves, Alps

1. INTRODUCTION

Sulfate reduction is one of the most important processes controlling the sulfur cycle; it can occur abiotically (by Thermochemical Sulfate Reduction, TSR), or be driven by biological activity (Microbial Sulfate Reduction, MSR; Machel, 2001). Although MSR generates lesser amounts of the reaction products than TSR, the overall mass balance of the reaction is identical for the two processes and can be approximated as (here, using methane as a reducing agent):

$$SO_4^{2-} + CH_4 \rightarrow H_2S + CO_2 + 2OH^-. \quad (1)$$

Apart from methane, the involvement of other reducing agents (e.g., hydrocarbons, Fe^{2+}, H_2) leads to different MSR and TSR reactions. In detail, the reaction is much more complex because numerous sulfur species of intermediate valence are involved throughout the transfer of eight electrons from sulfate to sulfide (Goldstein and Aizenshtat, 1994; Farquhar et al., 2007; Johnston et al., 2007; Sim et al., 2011; Truche et al., 2014, 2009; Barré et al., 2017). The two processes can occur sequentially during the diagenetic/tectonic history of a sedimentary basin, or separately accordingly to geological context. Indeed, MSR generally occurs during the early stages of diagenesis at T <80 °C (see review by Machel, 2001). As temperature increases during burial, sulfate-reducing bacteria cease to metabolize (Roussel et al., 2015) and TSR takes over at T >100–120 °C (Machel et al., 1995). The sulfur isotopic compositions ($\delta^{34}S$) of sulfate and reduced sulfur compounds (elemental sulfur and sulfides) have been used to distinguish TSR from MSR because each process induces specific sulfate-sulfide fractionations ($\Delta^{34}S_{SO_4^{2-}\text{-}S^{2-}} = \delta^{34}S_{SO_4^{2-}} - \delta^{34}S_{S^{2-}}$). In the case of MSR, such fractionations range from 15 to 72‰; this large range results from the heterogeneous isotopic fractionations associated with distinct sulfato-reducing bacteria that employ different metabolic pathways with various intermediate-valence sulfur species (Machel et al., 1995; Farquhar et al., 2007; Johnston et al., 2007; Sim et al., 2011; Labrado et al., 2019).

For TSR, the observed isotopic fractionation depends on temperature and it can be kinetically controlled or occur at isotopic equilibrium (e.g., Ohmoto and Lasaga, 1982). Kinetic isotopic fractionations are attributed to the initial rupture of the S-O bond in sulfate, resulting in the relative enrichment of ^{32}S (depletion of ^{34}S) in the reduced product and the depletion of ^{32}S (enrichment of ^{34}S) in the residual sulfate (e.g., Cross, 1999). Experimental studies have shown that kinetic effects lead to a maximum $\Delta^{34}S_{SO_4^{2-}\text{-}S^{2-}}$ value of 12.4‰ (e.g., Goldstein and Aizenshtat, 1994; Meshoulam et al., 2016, and references therein). In contrast, at isotopic equilibrium, theoretical calculations using the fractionation factor between SO_4^{2-} and H_2S_{aq} at various temperatures (Eldridge et al., 2016) indicate that $\Delta^{34}S_{SO_4^{2-}\text{-}S^{2-}}$ ranges from 11‰ at 500 °C to 43‰ at 100 °C. Because this range overlaps that observed for MSR, $\Delta^{34}S_{SO_4^{2-}\text{-}S^{2-}}$ values alone cannot indisputably discriminate TSR from MSR, whatever the origin of the fractionation (abiotic or biotic, equilibrium or kinetic). At present, additional petrographic and geochemical information is required to reliably identify TSR. Multiple sulfur isotopes analyses ($\delta^{33}S$, $\delta^{34}S$, $\delta^{36}S$) have been successfully used to better understand both the isotopic fractionation and the reaction pathways involved during the metabolism of sulfate-reducing bacteria (e.g., Farquhar et al., 2007; Johnston et al., 2007; Zerkle et al., 2009; Sim et al., 2011). However, this technique has not yet been used to characterize the multiple sulfur isotopes signature of the TSR reaction pathway, nor to attempt to discriminate it from that of MSR.

Here, we used multiple sulfur isotopes analysis ($\delta^{33}S$, $\delta^{34}S$, $\delta^{36}S$) as a promising geochemical tool to characterize the isotopic signature of TSR. This methodology allows both the robust determination of isotopic equilibrium and the calculation of mixing curves between different sulfur reservoirs. Finally, we explore the potential of TSR to generate sulfur mass independent fractionations (S-MIF) signatures. We focus on the “Nappe des Gypses”, a meta-evaporitic formation in the western French Alps. Our approach gives access to the temperatures at which

reduced phases precipitated and allows us to explain the S isotopic signatures of all the S-rich minerals observed.

2. THE NAPPE DES GYPSES FORMATION

The studied area encompasses seven evaporite outcrops in the western French Alps near the villages of Modane, Bramans, and Sollières-l'Envers (Arc Valley), the Ambin stream, the Mont-Cenis Lake, the Roubion stream (near Névache village), and Tignes Lake (Fig. 1). The Nappe des Gypses outcrops comprise 100–400 m of massive anhydrite deposits interbedded with dolomitic boudins, micaschists and black shales centimeter to meters in thickness. During the subduction-collision path of the Alps, the Nappe des Gypses formation acted as a major decollement that was crucial to the structuring of the Alps. The formation underwent three metamorphic and deformational events typical of the Alps (namely D1, D2, and D3), which favored fluid-rock interactions (see Barré et al., 2020, for a complete description of the tectonic evolution of the Nappe des Gypses). Sulfides (pyrite and minor chalcopyrite) and elemental sulfur (Fig. 2; Barré et al., 2017) are observed in direct association with anhydrite and recrystallized carbonates (Barré et al., 2020), corresponding to a typical TSR paragenesis (e.g., Machel et al., 1995). In addition, the characteristic intermediate-valence sulfur species required for TSR to occur, S_3^- and S_n^{2-} (polysulfides), have been identified by *in-situ* Raman analyses of heated fluid inclusions (Barré et al., 2017). Thus, all physico-chemical conditions necessary for TSR to occur were present in the Nappe des Gypses.

3. MATERIALS AND METHODS

3.1 Multiple sulfur isotopes notation

We performed multiple sulfur isotopes analyses by measuring $\delta^{33}S$, $\delta^{34}S$, and $\delta^{36}S$. All results are reported in the conventional δ^xS notation with respect to Vienna Cañon Diablo Troilite (V-CDT) as:

$$\delta^xS = ({}^xR_{sample} / {}^xR_{reference} - 1) \times 1000 \quad (‰) \qquad (2)$$

where x is the mass number of the sulfur isotope (33, 34, or 36) and R is the isotopic ratio $^{x}S/^{32}S$. The sulfur isotope fractionation factor between two compounds A and B (Hulston and Thode, 1965; Ono et al., 2006; Farquhar et al., 2007) is defined as:

$$^{x}\alpha_{A\text{-}B} = (\delta^{x}S_A + 1000) / (\delta^{x}S_B + 1000) \quad (3).$$

Isotopic fractionation between two minerals, here between the oxidized mineral (sulfate) and its reduced counterparts (sulfide or elemental sulfur), are calculated as:

$$\Delta^{34}S_{S\text{-}SO4} \approx \delta^{34}S_{\text{reduced S}} - \delta^{34}S_{\text{sulfate}} \quad (4)$$

Mass fractionation exponents are defined as:

$$^{x}\lambda_{A\text{-}B} = \ln(^{x}\alpha_{A\text{-}B}) / \ln(^{34}\alpha_{A\text{-}B}), \quad (5)$$

where x = 33 or 36.

These were calculated to determine potential sub-percent deviations from the conventional reference equilibrium values of 0.515 and 1.90 for $^{33}\lambda$ and $^{36}\lambda$, respectively (Hulston and Thodes, 1965; Ono et al., 2006; Farquhar et al., 2007; Eldridge et al., 2016). For most species, exponent values approaching 0.515 and 1.90 indicate an equilibrium process, whereas kinetic processes deviate from equilibrium values (Ono et al., 2006). These deviations can vary depending on the species present (Farquhar and Wing, 2003) and temperature (Otake et al., 2008). Note that, at isotopic equilibrium, $^{33}\lambda_{A\text{-}B}$ and $^{36}\lambda_{A\text{-}B}$ are conventionally written as $^{33}\theta_{A\text{-}B}$ and $^{36}\theta_{A\text{-}B}$, respectively, although the calculation does not differ from that in Eq. (5).

We used capital delta values defined as:

$$\Delta^{33}S = \delta^{33}S - [(\delta^{34}S / 1000 + 1)^{0.515} - 1] \times 1000 \quad (6)$$

and

$$\Delta^{36}S = \delta^{36}S - [(\delta^{34}S / 1000 + 1)^{1.90} - 1] \times 1000 \quad (7)$$

for a more convenient graphical representation and to facilitate discussion of subtle isotopic variations. Note that ^{36}S is a minor isotope (abundance 0.02%); consequently, the statistical error related to its measurement is greater than those for ^{33}S and ^{34}S.

3.2 Analytical procedure

Multiple sulfur isotopic analyses were performed separately on anhydrite, sulfides (pyrite or chalcopyrite), and elemental sulfur samples. Between 2 and 1,000 mg of powder of each mineral phase was collected using a Dremel tool to bore holes 1 or 2 mm in diameter. This allowed us to precisely target the desired mineral phases within <1 mm, regardless of the host environment. Sulfur was extracted from each phase by wet chemistry at the Centre de Recherches Pétrographiques et Géochimiques (CRPG, Vandœuvre-Lès-Nancy, France), following previously established species-specific protocols: (i) sulfides were extracted using 5 N HCl and a chromium-reduced sulfides (CRS) solution (Canfield et al., 1986); (ii) elemental sulfur was extracted using 5 N HCl and a CRS solution with added ethanol to optimize extraction yields (Gröger et al., 2009); and (iii) sulfates were extracted by adding a strongly reducing hydriodic hypophosphorous acid solution (Kitayama et al., 2017). In all cases, H_2S was liberated from the rock powder, converted into Ag_2S by reaction with an $AgNO_3$ solution, and cleaned with milli-Q water and dissolved ammonia. To determine the efficiency and repeatability of our sulfur extraction procedure, we performed preliminary extractions on pure phases (pyrite, elemental sulfur, anhydrite), which resulted in systematic conversion yields of 87–100%. Such high yields do not impact the measured isotopic compositions (Kitayama et al., 2017). We therefore assume that all our extractions from natural samples (i.e., non-pure phases) resulted in similar extraction yields that did not impact the isotopic compositions. This is confirmed by the good reproducibility of extractions and associated isotopic compositions for replicate analyses of a given same sample.

High-precision isotopic measurements by gas-source mass spectrometry require that the sample be analyzed as SF_6 to prevent any isobaric interference classically associated with SO_2 analyses (i.e., due to multiple O isotopes). The recovered Ag_2S was fluorinated in nickel reaction bombs by reaction with excess F_2 overnight at 250 °C to produce SF_6. After purification

using cryogenic traps and gas chromatography, the recovered SF_6 was introduced into a ThermoFinnigan MAT 253 dual-inlet gas-source mass spectrometer at the Institut de Physique du Globe de Paris (IPGP, France).

Standard deviations on isotopic analyses were estimated as the sum of the internal (corresponding to standard deviation during sample measurement by mass spectrometry) and external errors (corresponding to sulfur extraction and purification steps) after the complete extraction, fluorination, and measurement procedure, and after comparison with International Atomic Energy Agency (IAEA) Ag_2S standards S1 and S2. Standard deviations are better than 0.1‰, 0.01‰, and 0.1‰ for $\delta^{34}S$, $\Delta^{33}S$, and $\Delta^{36}S$, respectively.

4. RESULTS

4.1 Petrographic analysis

Sulfides (mostly pyrite and scarce texturally syngenetic chalcopyrite) are always observed in association with micaschist layers, occurring either as isolated grains/grain clusters in anhydrite facies (Fig. 2A–H–I) or as carbonate-quartz-sulfide veins in micaschists (Fig. 2D). When micaschists are absent, only elemental sulfur is observed, either well crystallized within fractures in gray dolomite sedimentary layers (often deformed as boudins; Fig. 2B) or in anhydrite deformation structures (Fig. 2C–E–F–G). Sulfides are only observed in centimeter-scale association with elemental sulfur in the presence of micaschist at the Sollières l'Envers outcrop (Fig. 2E).

4.2 S isotopic compositions of sulfate, sulfide, and elemental sulfur

We performed multiple sulfur isotopes analyses on 44 samples, comprising three mineral types collected across the six sampling sites: sulfates (anhydrite or gypsum), sulfides (pyrite or chalcopyrite), and elemental sulfur (Table 1). The sulfur isotopic compositions of sulfates and elemental sulfur are rather homogeneous across all six sites (Fig. 3). Anhydrite is enriched in ^{34}S ($\delta^{34}S_{anhydrite}$ = 12.74–18.39‰, mean 15.44 ± 1.53‰, all standard deviations reported as 1σ)

compared to elemental sulfur ($\delta^{34}S_{S_8}$ = −18.82 to −13.17‰, mean −15.40 ± 1.91‰), and both phases have small non-zero $\Delta^{33}S$ and $\Delta^{36}S$ values: for anhydrite, $\Delta^{33}S_{anhydrite}$ = 0.00–0.09‰ (mean 0.03 ± 0.03‰) and $\Delta^{36}S_{anhydrite}$ = −1.11 to +1.26‰ (mean −0.30 ± 0.69‰); for elemental sulfur, $\Delta^{33}S_{S_8}$ = 0.00–0.06‰ (mean 0.02 ± 0.02‰) and $\Delta^{36}S_{S_8}$ = −0.95 to +1.06‰ (mean 0.42 ± 0.68‰). Sulfides (without distinction between pyrite and chalcopyrite) display more variable compositions with $\delta^{34}S_{sulfide}$ = −5.44 to +11.60‰ (mean 3.14 ± 4.01‰) and near-zero values for both $\Delta^{33}S$ (0.00 ± 0.03‰) and $\Delta^{36}S$ (0.09 ± 0.54‰). No relationship was observed between sulfur isotopic composition and petrographic context (i.e., native sulfur in fractures or within the schistosity of anhydrite; sulfides disseminated in anhydrite or present in carbonate-quartz-sulfide veins associated with micaschist layers).

5. DISCUSSION

5.1 Triassic sulfate signatures

The $\delta^{34}S$ values of sulfates from the Nappe des Gypses range from 12.74 to 18.39‰, similar to ranges reported in evaporites of the Khuff Formation (Abu Dhabi; Worden et al., 1997) and in gas fields of Alberta (Yang et al., 2001). In both cases, the isotopic compositions were interpreted as being inherited from dissolved sulfate during seawater evaporation. The Upper Triassic age of the Nappe de Gypses evaporites was previously estimated by paleontological studies (Debelmas et al., 1989) and the mean isotopic composition of sulfates reported here ($\delta^{34}S$ =15.44 ± 1.53‰) is consistent with the sulfate signature of Carnian seawater (16.15 ± 1.03‰) recorded in anhydrite and gypsum from Israel and the Italian Alps (Fig. 3; Claypool et al., 1980; Crockford et al., 2019; and references therein). To our knowledge, the only coupled $\delta^{34}S$ and $\Delta^{33}S$ values reported for Carnian seawater are for samples of carbonate associated sulfate (CAS; i.e., traces of seawater sulfate incorporated during carbonate precipitation), with $\delta^{34}S$ = 20.84 ± 6.18‰ and $\Delta^{33}S$ = −0.01 ± 0.03‰ (Wu et al., 2014). These values agree well

222 with our data ($\delta^{34}S$ = 15.44 ± 1.53‰, $\Delta^{33}S$ = 0.03 ± 0.03‰) to which we add the first $\Delta^{36}S$
223 values for Carnian seawater: −0.30 ± 0.69‰.

224 **5.2 Abiotic formation mechanism of sulfide and elemental sulfur**

225 Previous studies of natural samples indicate that reduced sulfur minerals (subscript 'S'; i.e.,
226 sulfides or elemental sulfur) produced by TSR record isotopic fractionations of no more than
227 20‰ relative to their reactant sulfate (i.e., $\Delta^{34}S_{SO4\text{-}S} \geq 20‰$; e.g., Machel et al., 1995; Cross,
228 1999). Meshoulam et al. (2016, and references therein) experimentally determined that a
229 maximum fractionation of 12.4‰ between sulfates and sulfides ($\Delta^{34}S_{SO_4^{2-}\text{-}S^{2-}}$) should be
230 produced by kinetic effects during TSR alone. To our knowledge, only one study has reported
231 a $\Delta^{34}S_{SO_4\text{-}S}$ fractionation produced by TSR as high as 35‰ in natural samples (Alonso-Azcárate
232 et al., 2001); they attributed such a high $\Delta^{34}S_{SO_4\text{-}S}$ value to limited organic matter availability
233 and high rates of isotopic equilibration. Higher $\Delta^{34}S_{SO_4\text{-}S}$ values (up to 75‰) cannot be
234 explained by abiotic geological processes because of the low inferred temperature and would
235 thus generally result from MSR (e.g., Machel et al., 1995; Labrado et al., 2019).

236 Our results indicate that $\Delta^{34}S_{SO_4^{2-}\text{-}S^{2-}}$ values between anhydrite and associated sulfides range
237 from 4.2 to 20.4‰, consistent with TSR. In contrast, $\Delta^{34}S_{SO_4^{2-}\text{-}S_8}$ values between anhydrite and
238 associated elemental sulfur range from 28.1 to 33.3‰; a fractionation of such magnitude is
239 more ambiguous and could potentially record a biological input via MSR. Indeed, the presence
240 of elemental sulfur in salt dome caprocks and other evaporite settings is commonly explained
241 by the late oxidation of H_2S, which is generated either microbiologically (see review by
242 Labrado et al., 2019) or abiotically (e.g., Machel et al., 1995). The $\delta^{33}S$ value of elemental sulfur
243 can be used to differentiate between the two pathways. Indeed, equilibrium should lead to $\Delta^{33}S$
244 values near zero, whereas previous studies have reported systematic excesses of ^{33}S in reduced
245 MSR by-products, with $\Delta^{33}S$ values up to 0.2 ± 0.05‰ (and associated $\Delta^{34}S_{SO_4\text{-}S}$ values of 10–

75‰) relative to the initial sulfates (e.g., Farquhar et al., 2007; Zerkle et al., 2009; Johnston, 2011; Sim et al., 2011). In the present study, the $\Delta^{33}S$ values of elemental sulfur from all studies sites are 0.00–0.06‰, comparable to those of sulfates (0.00–0.09‰; Table 1, Fig. 4). Such similar values are not consistent with the production of elemental sulfur by a bacterial-mediated reaction mechanism; if that were the case, one would expect the $\Delta^{33}S$ values of elemental sulfur to be 0.05–0.2‰ greater than those of sulfates. Hence, our data are generally consistent with an equilibrium TSR process. Sulfides show $\Delta^{33}S$ values between −0.06 and +0.06‰ (Table 1, Fig. 4), slightly lower than those of sulfates. Moreover, the metamorphic path of the Nappe des Gypses formation was characterized by high temperatures of 137–431 °C throughout its history (Barré et al., 2020), and the occurrence of elemental sulfur in fractures and deformed anhydrite bedding (Fig. 2B, C, E) implies that it formed during the tectonic evolution of the Nappe des Gypses. Thus, H_2S cannot have been generated later by oxidation at the surface, again inconsistent with bacterial activity. This confirms that multiple sulfur isotopes can easily distinguish TSR from MSR, especially based on the $\Delta^{33}S$ signatures of the reduced by-products: TSR results in $\Delta^{33}S$ values equal or below those of the initial sulfate, whereas MSR leads to higher values.

5.3 No S-MIF generated during TSR

Multiple sulfur isotopes analyses are generally used to track photochemical reactions producing sulfur mass independent fractionations (S-MIFs; e.g., Farquhar et al., 2000; Johnston, 2011; Thomassot et al., 2015). Compared with common mass-dependent fractionations that produce zero to near-zero $\Delta^{33}S$ and $\Delta^{36}S$ values, S-MIFs correspond to anomalous $\Delta^{33}S$ and $\Delta^{36}S$ values that greatly depart from zero. Two studies have reported TSR experiments using concentrated amino acids as a reducing agent to produce significant S-MIFs. Watanabe et al. (2009) showed $\Delta^{33}S$ fractionations up to +2.1‰ with associated $\Delta^{36}S$ values between −1.1 and +1.1‰ in the amino acid residue; they attributed these fractionations to the

adsorption of S species on solid mineral surfaces and to a magnetic isotopic effect. Oduro et al. (2011) also attributed the large $\Delta^{33}S$ fractionation (up to +13.1‰) observed in the residue of their experiments to an ion-radical pair mechanism that would generate a magnetic isotopic effect on odd isotopes (i.e., ^{33}S), producing anomalous $\Delta^{33}S$ values whereas $\Delta^{36}S$ remains mass-dependent. They also concluded that TSR is not directly responsible for such fractionations because, so far, no study on natural samples has revealed a S-MIF specifically of odd isotopes.

Several studies have also speculated that the involvement of the radical ion S_3^- in the TSR process may contribute to anomalous sulfur isotopic compositions (Truche et al., 2014; Pokrovski and Dubessy, 2015; Barré et al., 2017) due to its interesting symmetry properties that are comparable to those of ozone which induces mass-independent oxygen isotopic fractionations (Michalski and Bhattacharya, 2009). However, recent experiments producing radical sulfur ions did not show any significant anomalies under the investigated conditions (Kokh et al., 2020), although their experiments did not directly correspond to TSR because their experimental setup did not involve a reducing agent. These experimental studies demonstrate that the different mechanisms associated with TSR process may or may not generate S-MIFs. Nonetheless, none of these experiments are representative of natural TSR conditions. It is therefore essential to identify the signature of TSR under natural conditions.

Only one study has documented S-MIF in natural sulfide samples for which TSR is suspected, showing $\Delta^{33}S$ values up to +1.25‰ in Paleoproterozoic shales (Young et al., 2013). However, Hu et al. (2020) showed that the reduction of sulfates with initial non-zero $\Delta^{33}S$ values will produce sulfides along a classical mass-dependent line, which will thus preserve the initial anomalous signature of the sulfates. Thus, the S-MIF observed by Young et al. (2013) in Paleoproterozoic black shales may result from the reduction of sulfates or the leaching of Archean sulfides that already exhibited non-zero $\Delta^{33}S$ values. Therefore, without direct

295 evidence of the occurrence of TSR in those rocks, it is impossible to prove that the observed S-
296 MIF truly results from TSR.

297 In our study of the Nappe des Gypses formation, despite the clear occurrence of TSR and the
298 presence of dissolved S_3^- as well as polysulfides (S_n^{2-}) in fluid inclusions heated above 200 °C
299 (Barré et al., 2017), we do not observe any significant S-MIF: $\Delta^{33}S_{anhydrite}$ = 0.03 ± 0.03‰,
300 $\Delta^{33}S_{sulfide}$ = 0.00 ± 0.03‰, and $\Delta^{33}S_{S_8}$ = 0.02 ± 0.02‰, and $\Delta^{36}S_{anhydrite}$ = −0.30 ± 0.69‰,
301 $\Delta^{36}S_{sulfide}$ = 0.09 ± 0.54‰, and $\Delta^{36}S_{S_8}$ = 0.42 ± 0.68‰ (Table 2). In conclusion, our results do
302 not evidence any TSR-driven mass-independent fractionation.

303 **5.4 Equilibrium vs. disequilibrium as reflected by isotopic composition**

304 The use of isotopic geothermometers based on the fractionation factor between two
305 syngenetic chemical species requires that they be in isotopic equilibrium. In most cases, this
306 requirement is inferred based on petrographic observations. When two mineral species appear
307 to be syngenetic, it is considered that they are at isotopic equilibrium. Jamieson et al. (2006)
308 used multiple sulfur isotopes analyses to investigate the isotopic equilibrium between sulfide
309 pairs (i.e., two sulfide species considered to be syngenetic) based on their respective $\delta^{34}S$ and
310 $\Delta^{33}S$ values. They showed that, given geological context and depending on the phases involved,
311 two minerals with different $\delta^{34}S$ values but similar $\Delta^{33}S$ values are considered to be at isotopic
312 equilibrium. By following a similar approach in our case study, it is possible to demonstrate if
313 the reduced sulfur minerals and sulfates are truly at isotopic equilibrium.

314 Here, we used $^{34}S/^{32}S$ fractionation factors at relevant temperatures between aqueous sulfates
315 and aqueous H_2S from Eldridge et al. (2016) and between aqueous sulfates and aqueous
316 elemental sulfur (S_8) from Eldridge et al. (2021) to determine the equilibrium temperatures of
317 the different reduced sulfur compounds (Table 2). Using this method, the apparent precipitation
318 temperatures of some sulfides are higher (up to 980 °C; Table 2) than the metamorphic peak
319 temperature of the Nappe des Gypses formation (431 ± 28 °C; Barré et al., 2020) despite

320 petrographic criteria indicating the phases to be syngenetic (Fig. 2). This implies that
321 petrographic observations are not always a robust diagnostic tool for evaluating isotopic
322 equilibrium.

323 Fortunately, the relationships between the $^{33/32}S$, $^{34/32}S$ and $^{36/32}S$ fractionations (i.e., the mass
324 fractionation exponents λ) can be used as an independent test of whether two species are in
325 isotopic equilibrium. We determined the mass-fractionation exponents $^{33}\lambda$ and $^{36}\lambda$
326 (corresponding to the slopes of mass-dependent signatures in the $\delta^{33}S$ vs. $\delta^{34}S$ and $\delta^{36}S$ vs. $\delta^{34}S$
327 diagrams, respectively) between sulfates and the associated reduced forms (elemental sulfur or
328 sulfides) observed at each studied site (Table 2). We then further compared these mass-
329 fractionation exponents, associated with their previously determined equilibrium temperatures,
330 to those derived from theoretical calculations (Otake et al., 2008; Eldridge et al., 2016; Eldridge
331 et al., 2021). Considering the different sulfur species observed (H_2S_{aq}, SO_3^{2-}, S_8, S_3^-, S_n^{2-} and
332 CS_{2aq}), theoretical calculations give $^{33}\theta$ values (i.e., $^{33}\lambda$ at isotopic equilibrium) between 0.5143
333 and 0.5158 and $^{36}\theta$ values (i.e., $^{36}\lambda$ at isotopic equilibrium) between 1.8783 and 1.9223 for
334 temperatures of 25–1000 °C (Fig. 5). We note that, when plotting $\delta^{33}S$ vs. $\delta^{34}S$ and $\delta^{36}S$ vs.
335 $\delta^{34}S$, larger $\Delta^{34}S$ values (i.e., lower temperatures), provide more precise values of $^{33}\lambda$ and $^{36}\lambda$;
336 this is why the errors on λ values are larger at higher temperatures than at lower temperatures.
337 For that reason, λ values associated with high uncertainties cannot be used to demonstrate or
338 infer isotopic equilibrium. This implies that the determination of the mass fractionation
339 exponents mainly depends on the analytical precision and associated error on $\delta^{33}S$, $\delta^{34}S$ and
340 $\delta^{36}S$. Here, we use only the $^{33}\lambda$ values to determine if a mineral pair is consistent with isotopic
341 equilibrium because the precision on ^{36}S measurements is lower than that for ^{33}S; the $^{36}\lambda$ values
342 presented in Table 2 are included only to broaden the published dataset. We consider a mineral
343 pair to be at isotopic equilibrium only if the associated $^{33}\lambda$ value is between 0.5140 and 0.5170;
344 only in that case do we consider the associated equilibrium temperature (Fig. 5).

Elemental sulfur at isotopic equilibrium. The mass-fractionation exponents between sulfates and elemental sulfur ($^{33}\lambda_{SO_4\text{-}S_8}$) at all analyzed sites are between 0.51467 and 0.51632 (Table 2, Fig. 5), implying that sulfates and all elemental sulfur samples are consistent with isotopic equilibrium. Their corresponding equilibrium temperatures are in the range 172–217 °C (Table 2, Fig. 5). These temperatures correspond to the liquid-solid phase transition of elemental sulfur at the lowest P-T conditions recorded by the Nappe des Gypses formation (Fig. 6; Barré et al., 2020). This result implies with a unique P-T condition at which all elemental sulfur throughout the formation precipitated at the same time, which accounts for the similar isotopic signatures of all the analyzed samples. Interestingly, fluid inclusions from this evaporitic formation contain tiny crystals of elemental sulfur, in addition to sulfates and sulfides that are dissolved in the brines at room temperature. This elemental sulfur disproportionates when heating the fluid inclusions to >200 °C and significant concentrations (milli-molar range) of polysulfides (including the S_3^- radical ion) were measured by *in-situ* Raman spectroscopy (Barré et al., 2017). This indicates that elemental sulfur precipitates directly from the recombination of dissolved polysulfides (Steudel and Chivers, 2019) involved in TSR (Barré et al., 2017). Consequently, the elemental sulfur, as collected herein from the Nappe des Gypses formation, records the TSR-driven isotopic signatures of the polysulfides from which it formed.

Sulfides at isotopic equilibrium. Based on the mass-fractionation exponents calculated between sulfates and sulfides ($^{33}\lambda_{SO_4\text{-}H_2S}$), only three of eleven samples are consistent with equilibrium isotopic exchange reactions: two pyrites from the Sollières and Ambin outcrops and one chalcopyrite from the Mont-Cenis Lake outcrop (Fig. 4C–E). Their equilibrium temperatures are 293 ± 20 °C, 344 ± 20 °C, and 488 ± 55 °C, respectively (Table 2, Fig. 5), consistent with the kinetics of the isotopic equilibrium between SO_4^{2-} and H_2S, which is attained within a few days at >350 °C (Ohmoto and Lasaga, 1982). These temperatures match well with the D2-D3 transition phase (259 ± 24 °C), the D1-D2 transition (350 ± 20 °C), and

the peak metamorphic temperature (431 ± 28 °C) of the Nappe des Gypses formation, respectively (Barré et al., 2020). This result suggests that TSR occurred at least from the metamorphic peak to the D2-D3 transition phase during the exhumation of the host formation.

All other samples present $^{33}\lambda_{SO_4\text{-}H_2S}$ values between 0.517 and 0.523, i.e., significantly deviating from the estimated isotopic equilibrium range (Fig. 5). They cannot be at isotopic equilibrium, and therefore their derived "equilibrium temperatures" are not considered further. This means that another process was involved in their precipitation, as discussed in the following subsection.

5.5 Evidence of mixing between sulfates and elemental sulfur

In this subsection, we focus on the eight sulfide samples with $^{33}\lambda_{SO_4\text{-}H_2S}$ values of 0.517–0.523 that deviate significantly from the theoretical equilibrium value of 0.515 (Table 2, Fig. 5). Such deviations could reflect kinetically controlled S fractionation during sulfide precipitation. However, kinetic mechanisms generally involve percent-level deviations towards values below that of isotopic equilibrium (Ono et al., 2006); for oxygen isotopes, for example, the λ value can be lowered from the equilibrium value by 0.027 in an abiotic reaction (Clayton and Mayeda, 2009). Here, the $^{33}\lambda$ values deviate from the previously determined isotopic equilibrium range (0.5148–0.5163) by +0.0021 to +0.0080. Because these values are higher than those at equilibrium, it is unlikely that they result from simple, unidirectional mechanisms. Alternatively, mixing between two reservoirs might explain such observations. To test this hypothesis, we performed two-component mixing calculations on $\delta^{34}S$, $\Delta^{33}S$, and $\Delta^{36}S$. In our calculation, mixing between two pools occurs in the aqueous phase and the resulting isotopic composition derives from the proportion of each species in the fluid. Because TSR occurs in solution, mixing is possible between any two of the various sulfur species involved in the reaction (i.e., sulfates, sulfides, elemental sulfur, polysulfides, organic sulfur species, and other

394 minor intermediate-valence species; Goldstein and Aizenshtat, 1994; Meshoulam et al., 2016;
395 Barré et al., 2017).

396 The sulfur reservoirs considered here are (1) dissolved Triassic sulfates, (2) elemental sulfur
397 (corresponding to polysulfides dissolved in the hot fluid formed at isotopic equilibrium; see
398 section 5.4), and (3) dissolved organic sulfur. Regarding the latter, evaporites of Upper Triassic
399 (Carnian) age are known to present sedimentation conditions with high potential for sulfur-rich
400 kerogen deposition (Cota and Baric, 1998). During the burial and exhumation history of the
401 formation, these sulfur-rich kerogens can experience thermal cracking, releasing organic sulfur
402 species into the fluid. Here, stromatolitic dolomites and black shales are observed in the Nappe
403 des Gypses formation (Barré et al., 2020), which are good candidates for sedimentary facies
404 containing S-rich kerogen. However, the kerogen in these rocks is too thermally mature to
405 expect any preservation of organic sulfur, precluding the direct determination of its isotopic
406 composition. Therefore, we used a theoretical organic S reservoir with a $\delta^{34}S$ signature of
407 −30‰, consistent with values reported for the organic sources of H_2S in several sour gas fields
408 (Werne et al., 2004, and references therein). We note that, because anhydrite is present in large
409 excess compared to the other sulfur species, we consider sulfates as an infinite reservoir. The
410 sulfate isotopic signature therefore remains constant throughout our calculation of the
411 geological history of the Nappe des Gypses.

412 Mixing curves between sulfates and elemental sulfur (or organic sulfur) are calculated as:

413 $$\left(\frac{\delta^{x}S_{mix}}{1000}+1\right)=\left(\frac{\delta^{x}S_{S_8}}{1000}+1\right)\times\chi_{S8}+\left(\frac{\delta^{x}S_{SO_4}}{1000}+1\right)\times\chi_{SO4} \quad (8)$$

414 where x = 33, 34, or 36, χ_{S8} and χ_{SO4} are the proportions (between 0 and 1) of elemental sulfur
415 (S_8; or organic sulfur) and sulfate (SO_4), respectively, and $\delta^{x}S_{mix}$ is the isotopic value obtained
416 by mixing of the measured sulfate and elemental sulfur compositions. The associated $\Delta^{33}S$ and
417 $\Delta^{36}S$ values are then deduced from $\delta^{x}S_{mix}$ using Eqs. (6) and (7). We note that in the $\Delta^{33}S$ vs.
418 $\delta^{34}S$ and $\Delta^{36}S$ vs. $\Delta^{33}S$ diagrams (Figs. 4 and 7, respectively), a mixture between two reservoirs

corresponds to a curve, instead of a line as in a δ vs. δ diagram. For mixing to be a viable hypothesis, both the $\Delta^{33}S$ and $\Delta^{36}S$ values of the sulfides must be satisfactorily explained.

Mixing between sulfate and elemental sulfur. In this study, sulfides have $\Delta^{33}S$ values that are equal or lower than those of associated sulfate and elemental sulfur, and $\delta^{34}S$ values between +11.60 and −0.30‰. The obtained mixing curves are illustrated in the $\Delta^{33}S$ vs. $\delta^{34}S$ and $\Delta^{33}S$ vs. $\Delta^{36}S$ diagrams (Figs. 4 and 7, respectively), showing that most of the sulfides (five of eight samples) are consistent with mixing between sulfate and elemental sulfur (representing dissolved polysulfides) to produce H_2S, the latter two species being generated during TSR. The mixing curves allow us to determine the relative proportions of each isotopic reservoir recorded by a single sulfide. Here, the proportion of elemental sulfur (i.e., dissolved polysulfides at higher temperature) ranges between 18 and 50% (mean 33 ± 10%), in good agreement with the proportion of dissolved polysulfides measured in fluid inclusions from the Nappe des Gypses formation, which can represent up to 25% of the total dissolved sulfur concentration in the fluid at 300 °C (Barré et al., 2017), and probably more at higher temperature (Pokrovski and Dubessy, 2015). Given a mixture of 33% elemental sulfur ($\delta^{34}S$ = −15.40 ± 1.91‰, $\Delta^{33}S$ = 0.016 ± 0.018‰, $\Delta^{36}S$ = 0.421 ± 0.680‰) with 67% sulfate ($\delta^{34}S$ = 15.44 ± 1.53‰, $\Delta^{33}S$ = 0.033 ± 0.027‰, $\Delta^{36}S$ = −0.297 ± 0.690‰), our calculation predicts the resulting sulfide isotopic composition to be $\delta^{34}S$ = −2.33 ± 2.35‰, $\Delta^{33}S$ = −0.0030 ± 0.0011‰, and $\Delta^{36}S$ = 0.1826 ± 0.0685‰. These values are very similar to the mean values measured in the observed sulfides ($\delta^{34}S$ = 3.14 ± 4.01‰, $\Delta^{33}S$ = −0.0025 ± 0.0316‰, $\Delta^{36}S$ = 0.0873 ± 0.5423‰; Fig. 8). This result is consistent with previous reports that isotopic exchanges between polysulfides and H_2S are extremely fast, even at room temperature, and that solid sulfides record up to 31% of the isotopic signature of the polysulfides from which they formed (Fossing and Jørgensen, 1990; Fossing et al., 1992). Therefore, we conclude that the isotopic compositions of the observed sulfides represent the mixture of ~67% sulfate signature with ~33% elemental sulfur

signature (i.e., dissolved polysulfides at temperature) at conditions corresponding to isotopic equilibrium.

Mixing between sulfate and organic sulfur. At Névache and Bramans, three sulfides present $\Delta^{33}S$ values slightly lower than those at the other localities (Fig. 4A, B) but consistent with mixing between sulfate and elemental sulfur, considering the 1σ error. However, taken together, their $\Delta^{33}S$ and $\Delta^{36}S$ values are not consistent with mixing between sulfates and elemental sulfur (Fig. 7A, B), implicating another sulfur reservoir. For these three samples, we assumed mixing between sulfate and a theoretical organic sulfur reservoir (again with $\delta^{34}S = -30‰$, see above). We estimated the $\Delta^{33}S$ and $\Delta^{36}S$ values of organic sulfur (using $^{33}\lambda = 0.5152$ and $^{36}\lambda = 1.89$) that reproduce the three samples in both the $\Delta^{33}S$ vs. $\delta^{34}S$ and $\Delta^{33}S$ vs. $\Delta^{36}S$ diagrams. We obtained relative mixing proportions of organic sulfur of 28% at Névache and 22% at Bramans.

The good correlation between the mixing curves in both the $\Delta^{33}S$ vs. $\delta^{34}S$ and $\Delta^{33}S$ vs. $\Delta^{36}S$ diagrams is consistent with the sulfur sources belonging to the Nappe des Gypses formation, and no other process than TSR is required. Because the observed compositions do not require an exogenous sulfur-rich fluid, the sulfides must have formed in a closed system. As mixing occurs in the aqueous phase, this implies that all sulfides precipitated before elemental sulfur crystallized, and that TSR probably ceased after the D2-D3 transition during cooling (corresponding to a change in tectonic regime that lead the last exhumation step of the Nappe des Gypses formation; Barré et al., 2020).

5.6 Implications for the TSR mechanism

Our multiple sulfur isotopes results complement studies on MSR (e.g., Farquhar et al., 2007; Johnston et al., 2007; Zerkle et al., 2009; Sim et al., 2011) and show that TSR and MSR can be unambiguously discriminated based on the near zero to slightly negative (TSR) and positive (MSR) $\Delta^{33}S$ values of all participating reduced sulfur-bearing phases. This geochemical tool can therefore prove extremely useful for better deciphering the sulfur cycle in contexts where

the occurrence of the two processes is debated (e.g., petroleum systems, ore deposits, hydrothermal settings).

These results also provide a new understanding of the TSR reaction pathway and associated isotopic exchanges. The fluids of the Nappe des Gypses formation are considered to have been in a closed system because they mainly correspond to gypsum dehydration and connate seawater without the involvement of external fluid (Grappin et al., 1979). This implies that TSR products in a closed system may or may not be at isotopic equilibrium with a single fluid under similar conditions, which can be explained by the variable availability of dissolved metals. Here, iron was released at different stages of the Nappe des Gypses metamorphic path (Barré et al., 2020), implying a variable metal concentration in the fluid through time. When the metal concentration is sufficiently high, all the H_2S precipitates and no intermediate-valence sulfur species (i.e., polysulfides, S_3^-) remain in the fluid because they are only stable when both sulfates and sulfides are in solution (Truche et al., 2014; Pokrovski and Dubessy, 2015; Barré et al., 2017). In this case, the fractionation between sulfate and precipitating sulfide is temperature dependent and occurs at isotopic equilibrium. In contrast, if H_2S is in excess with respect to dissolved metals, only some H_2S would precipitate. The resulting sulfide mineral would thus have an isotopic composition corresponding to mixing between the dissolved sulfur species (sulfates and polysulfides; Fig. 8), facilitated by the rapid isotopic exchange between polysulfides and H_2S (Fossing and Jørgensen, 1990). The variable availability of metal in the system thus offers a plausible explanation for the distinct isotopic compositions of sulfides from the same geological context and involving only one fluid during TSR.

6. CONCLUSIONS

We presented a multiple sulfur isotopes analysis of coexisting sulfates, elemental sulfur, and sulfides in the Nappe des Gypses formation to characterize the reaction pathway of TSR and distinguish TSR from MSR. Our main conclusions are:

1. Multiple sulfur isotopes analysis can unambiguously differentiate TSR from MSR. Whereas MSR produces sulfide by-products with $\Delta^{33}S$ values above those of reacted sulfates, TSR produces sulfides with similar or lower $\Delta^{33}S$ values (down to −0.08‰).
2. We used mass-fractionation exponents ($^{33}\lambda$ and $^{36}\lambda$) to determine if S-bearing mineral pairs (sulfate-elemental sulfur or sulfate-sulfide) were at isotopic equilibrium. We demonstrate that this technique is far more robust than petrographic observations of syngenetic relationships to resolve this crucial point for isotopic geothermometry. We also determined and validated the precipitation temperatures of TSR by-products (i.e., pyrite, chalcopyrite, or elemental sulfur) based on the ^{34}S fractionation factors between aqueous sulfates and reduced S species (sulfides or polysulfides). Interestingly, elemental sulfur precipitated between 172 and 217 °C, temperatures that correspond to the elemental sulfur liquid-solid phase transition at the lowest *P-T* conditions recorded in the Nappe des Gypses formation.
3. Multiple sulfur isotopes analysis also allows interpretation of the isotopic compositions of all sulfides that are not at isotopic equilibrium. Whereas kinetic effects cannot explain these signatures, the two-component mixing calculations show that sulfides precipitated from a mixture between either sulfates and elemental sulfur (i.e., polysulfides at >200°C) or sulfates and organic sulfur. The obtained mixing curves show that the sulfide compositions are best reproduced by the mixing of 67% sulfates and 33% elemental sulfur, consistent with the proportion of dissolved polysulfides measured at >200 °C in fluid inclusions from the Nappe des Gypses formation (Barré et al., 2017).
4. We observed no evidence of S-MIF, even though we demonstrated the occurrence of TSR and investigated three S-bearing phases (sulfate, sulfide, and elemental sulfur) at isotopic equilibrium.

This study opens new perspectives for improving our understanding of the sulfur cycle, especially TSR-related hydrothermal-metamorphic ores or sour gas fields. The multiple sulfur isotopic approach can be used to discriminate MSR from TSR; its systematic application and careful interpretation of the obtained results will improve our understanding of both the isotopic fractionations and the reaction pathways involved in TSR.

Acknowledgements

This work was funded by LABEX ANR-10-LABX-21-01 Ressources21 (Strategic metal resources of the 21st Century), the French Ministry of Higher Education and Research, and the project Dear_Sir (ANR-15-CE31-0005). The authors would like to thank Robert Dennen who improved the fluidity and grammar of the paper. The paper was greatly improved thanks to relevant and detailed reviews by Simon Bottrell, two anonymous reviewers, and editorial support by Timothy Lyons.

References

Alonso-Azcárate, J., Bottrell, S.H., Tritlla, J., 2001. Sulfur redox reactions and formation of native sulfur veins during low grade metamorphism of gypsum evaporites, Cameros Basin (NE Spain). Chem. Geol. 174(4), 389-402.

Barré, G., Strzerzynski, P., Michels, R., Guillot, S., Cartigny, P., Thomassot, E., Lorgeoux, C., Assayag, N., Truche, L., 2020. Tectono-metamorphic evolution of an evaporitic décollement as recorded by mineral and fluid geochemistry: The “Nappe des Gypses” (Western Alps) case study. Lithos, 358, 105419.

Barré, G., Truche, L., Bazarkina, E.F., Michels, R., Dubessy, J., 2017. First evidence of the trisulfur radical ion S_3^- and other sulfur polymers in natural fluid inclusions. Chem. Geol. 462, 1-14.

Canfield, D.E., Raiswell, R., Westrich, J.T., Reaves, C.M., Berner, R.A., 1986. The use of chromium reduction in the analysis of reduced inorganic sulfur in sediments and shales. Chem. Geol. 54(1-2), 149-155.

Claypool, G.E., Holser, W.T., Kaplan, I.R., Sakai, H., Zak, I., 1980. The age curves of sulfur and oxygen isotopes in marine sulfate and their mutual interpretation. Chem. Geol. 28, 199-260.

Clayton, R.N., Mayeda, T.K., 2009. Kinetic isotope effects in oxygen in the laboratory dehydration of magnesian minerals. J. Phys. Chem. A, 113(10), 2212-2217.

Cota, L., Baric, G., 1998. Petroleum potential of the Adriatic offshore, Croatia. Org. Geochem. 29(1-3), 559-570.

Crapanzano, L. (2005). Polymorphism of sulfur: structural and dynamical aspects (Doctoral dissertation, Université Joseph-Fourier-Grenoble I).

Crockford, P.W., Kunzmann, M., Bekker, A., Hayles, J., Bao, H., Halverson, G.P., Peng, Y., Bui, T.H., Cox, G.M., Gibson, T.M., Wörndle, S., Rainbird, R., Lepland, A., Swanson-Hysell, N.L., Master, S., Sreenivas, B., Kuznetsov, A., Krupenik, V., Wing, B.A., 2019. Claypool continued: Extending the isotopic record of sedimentary sulfate. Chem. Geol., 513, 200-225.

Cross, M.M., 1999. Rates and mechanisms of thermochemical sulphate reduction (Doctoral dissertation, Manchester University).

Debelmas, J., Desmons, J., Ellenberger, F., Goffé, B., Fabre, J., Jaillard, E., and Pachoud, A., 1989. Notice explicative de la feuille Modane. B.R.G.M., scale 1/50 000, 1 sheet, 53 p. text (in french).

Eldridge, D.L., Guo, W., Farquhar, J., 2016. Theoretical estimates of equilibrium sulfur isotope effects in aqueous sulfur systems: Highlighting the role of isomers in the sulfite and sulfoxylate systems. Geochim. Cosmochim. Acta 195, 171-200.

Eldridge, D.L., Kamyshny Jr, A., Farquhar, J., 2021. Theoretical estimates of equilibrium sulfur isotope effects among aqueous polysulfur and associated compounds with applications to authigenic pyrite formation and hydrothermal disproportionation reactions. Geochim. Cosmochim. Acta 310, 281-319.

Farquhar, J., Bao, H., Thiemens, M., 2000. Atmospheric influence of Earth's earliest sulfur cycle. Science 289(5480), 756-758.

Farquhar, J., Johnston, D.T., Wing, B.A., 2007. Implications of conservation of mass effects on mass-dependent isotope fractionations: influence of network structure on sulfur isotope phase space of dissimilatory sulfate reduction. Geochim. Cosmochim. Acta 71(24), 5862-5875.

Farquhar, J., Wing, B.A., 2003. Multiple sulfur isotopes and the evolution of the atmosphere. Earth Planet. Sci. Lett. 213(1), 1-13.

Fossing, H., Jørgensen, B.B., 1990. Isotope exchange reactions with radiolabeled sulfur compounds in anoxic seawater. Biogeochemistry 9(3), 223-245.

Fossing, H., Thode-Andersen, S., Jørgensen, B.B., 1992. Sulfur isotope exchange between 35S-labeled inorganic sulfur compounds in anoxic marine sediments. Marine Chemistry 38(1-2), 117-132.

Goldstein, T.P., Aizenshtat, Z., 1994. Thermochemical sulfate reduction: A review. J. Therm. Anal. 42, 241-290.

Grappin, C., Saliot, P., Sabouraud, C., Touray, J.C., 1979. Les variations des rapports Cl/Br, Na/Br et K/Br dans les inclusions fluides des quartz de la cicatrice évaporitique de Bramans-Termignon (Vanoise, Alpes françaises). Chem. Geol. 25(1-2), 41-52.

Gröger, J., Franke, J., Hamer, K., Schulz, H.D., 2009. Quantitative recovery of elemental sulfur and improved selectivity in a chromium-reducible sulfur distillation. Geostand. Geoanal. Res. 33(1), 17-27.

591 Hu, D., Li, M., Zhang, X., Turchyn, A.V., Gong, Y., Shen, Y., 2020. Large mass-independent
592 sulphur isotope anomalies link stratospheric volcanism to the Late Ordovician mass
593 extinction. Nature communications, 11(1), 1-8.
594 Hulston, J.R., Thode, H.G., 1965. Variations in the S33, S34, and S36 contents of meteorites
595 and their relation to chemical and nuclear effects. J. Geophys. Res. 70(14), 3475-3484.
596 Jamieson, J.W., Wing, B.A., Hannington, M.D., Farquhar, J., 2006. Evaluating isotopic
597 equilibrium among sulfide mineral pairs in Archean ore deposits: case study from the Kidd
598 Creek VMS deposit, Ontario, Canada. Econ. Geol. 101(5), 1055-1061.
599 Johnston, D.T., 2011. Multiple sulfur isotopes and the evolution of Earth's surface sulfur cycle.
600 Earth-Sci. Rev. 106(1), 161-183.
601 Johnston, D.T., Farquhar, J., Canfield, D.E., 2007. Sulfur isotope insights into microbial sulfate
602 reduction: when microbes meet models. Geochim. Cosmochim. Acta 71(16), 3929-3947.
603 Kitayama, Y., Thomassot, E., Galy, A., Golovin, A., Korsakov, A., d'Eyrames, E., Assayag, N.,
604 Bouden, N. Ionov, D., 2017. Co-magmatic sulfides and sulfates in the Udachnaya-East pipe
605 (Siberia): A record of the redox state and isotopic composition of sulfur in kimberlites and
606 their mantle sources. Chem. Geol. 455, 315-330.
607 Kokh, M.A., Assayag, N., Mounic, S., Cartigny, P., Gurenko, A., Pokrovski, G.S., 2020.
608 Multiple sulfur isotope fractionation in hydrothermal systems in the presence of radical
609 ions and molecular sulfur. Geochim. Cosmochim. Acta 285, 100-128.
610 Labrado, A.L., Brunner, B., Bernasconi, S.M., Peckmann, J., 2019. Formation of large native
611 sulfur deposits does not require molecular oxygen. Front. Microbiol. 10, 24.
612 Machel, H.G., 2001. Bacterial and thermochemical sulfate reduction in diagenetic settings –
613 old and new insights. Sediment. Geol. 140, 143-175.
614 Machel, H.G., Krouse, H.R., Sassen, R., 1995. Products and distinguishing criteria of bacterial
615 and thermochemical sulfate reduction. Appl. Geochem. 10(4), 373-389.

616 Meshoulam, A., Ellis, G.S., Ahmad, W.S., Deev, A., Sessions, A.L., Tang, Y., Adkins, J.F.,
617 Jinzhong, L., Gilhooly, W.P., Aizenshtat, Z., Amrani, A., 2016. Study of thermochemical
618 sulfate reduction mechanism using compound specific sulfur isotope analysis. Geochim.
619 Cosmochim. Acta 188, 73-92.
620 Michalski, G., Bhattacharya, S.K., 2009. The role of symmetry in the mass independent isotope
621 effect in ozone. Proc. Natl. Acad. Sci. U.S.A. 106(14), 5493-5496.
622 Oduro, H., Harms, B., Sintim, H.O., Kaufman, A.J., Cody, G., Farquhar, J., 2011. Evidence of
623 magnetic isotope effects during thermochemical sulfate reduction. Proc. Natl. Acad. Sci.
624 U.S.A. 108, 17635-17638.
625 Ohmoto, H., Lasaga, A.C., 1982. Kinetics of reactions between aqueous sulfates and sulfides
626 in hydrothermal systems. Geochim. Cosmochim. Acta, 46(10), 1727-1745.
627 Ono, S., Wing, B., Johnston, D., Farquhar, J., Rumble, D., 2006. Mass-dependent fractionation
628 of quadruple stable sulfur isotope system as a new tracer of sulfur biogeochemical cycles.
629 Geochim. Cosmochim. Acta 70(9), 2238-2252.
630 Otake, T., Lasaga, A.C., Ohmoto, H., 2008. Ab initio calculations for equilibrium fractionations
631 in multiple sulfur isotope systems. Chem. Geol. 249(3), 357-376.
632 Pokrovski, G.S., Dubessy, J., 2015. Stability and abundance of the trisulfur radical ion S_3^- in
633 hydrothermal fluids. Earth Planet. Sci. Lett. 411, 298-309.
634 Roussel, E.G., Cragg, B.A., Webster, G., Sass, H., Tang, X., Williams, A.S., Gorra, R.,
635 Weightman, A.J., Parkes, R.J., 2015. Complex coupled metabolic and prokaryotic
636 community responses to increasing temperatures in anaerobic marine sediments: critical
637 temperatures and substrate changes. FEMS microbiology ecology, 91(8), fiv084.
638 Sim, M.S., Bosak, T., Ono, S., 2011. Large sulfur isotope fractionation does not require
639 disproportionation. Science, 333(6038), 74-77.

640 Steudel, R., Chivers, T., 2019. The role of polysulfide dianions and radical anions in the
641 chemical, physical and biological sciences, including sulfur-based batteries. Chem. Soc.
642 Rev. 48(12), 3279-3319.
643 Thomassot, E., O'Neil, J., Francis, D., Cartigny, P., Wing, B.A., 2015. Atmospheric record in
644 the Hadean Eon from multiple sulfur isotope measurements in Nuvvuagittuq Greenstone
645 Belt (Nunavik, Quebec). Proc. Natl. Acad. Sci. U.S.A. 112(3), 707-712.
646 Truche, L., Bazarkina, E.F., Barré, G., Thomassot, E., Berger, G., Dubessy, J., Robert, P., 2014.
647 The role of S_3^- ion in thermochemical sulphate reduction: Geological and geochemical
648 implications. Earth Planet. Sci. Lett. 396, 190-200.
649 Truche, L., Berger, G., Destrigneville, C., Pages, A., Guillaume, D., Giffaut, E. Jacquot, E.,
650 2009. Experimental reduction of aqueous sulphate by hydrogen under hydrothermal
651 conditions: implication for the nuclear waste storage. Geochim. Cosmochim. Acta,
652 *73*(16), 4824-4835.
653 Watanabe, Y., Farquhar, J., Ohmoto, H., 2009. Anomalous fractionations of sulfur isotopes
654 during thermochemical sulfate reduction. Science 324, 370-373.
655 Werne, J.P., Hollander, D.J., Lyons, T.W., Damsté, J.S.S., 2004. Organic sulfur
656 biogeochemistry: recent advances and future research directions. Geol. S. Am. S. 379, 135-
657 150.
658 Worden, R.H., Smalley, P.C., Fallick, A.E., 1997. Sulfur cycle in buried evaporites. Geology,
659 25, 643-646.
660 Wu, N., Farquhar, J., Strauss, H., 2014. $\delta^{34}S$ and $\Delta^{33}S$ records of Paleozoic seawater sulfate
661 based on the analysis of carbonate associated sulfate. Earth Planet. Sci. Lett. 399, 44-51.
662 Yang, C., Hutcheon, I., Krouse, H.R., 2001. Fluid inclusion and stable isotopic studies of
663 thermochemical sulphate reduction from Burnt Timber and Crossfield East gas fields in
664 Alberta, Canada. Bull. Can. Petrol. Geol. 49(1), 149-164.

Young, S.A., Loukola-Ruskeeniemi, K., Pratt, L.M., 2013. Reactions of hydrothermal solutions with organic matter in Paleoproterozoic black shales at Talvivaara, Finland: Evidence from multiple sulfur isotopes. Earth Planet. Sci. Lett. 367, 1-14.

Zerkle, A.L., Farquhar, J., Johnston, D.T., Cox, R.P., Canfield, D.E., 2009. Fractionation of multiple sulfur isotopes during phototrophic oxidation of sulfide and elemental sulfur by a green sulfur bacterium. Geochim. Cosmochim. Acta 73(2), 291-306.

TABLE CAPTIONS

Table 1. Multiple sulfur isotopes compositions of sulfur-bearing minerals from each studied site. Here, σ corresponds to analytical uncertainty.

Table 2. $^{33}\lambda$ and $^{36}\lambda$ values calculated between sulfates and either associated elemental sulfur (S_8), pyrite, or chalcopyrite. When the $^{33}\lambda$ value is between 0.5140 and 0.5170, we assume that isotopic equilibrium was attained and therefore that the associated apparent equilibrium temperature, determined using the respective $\Delta^{34}S$ values and SO_4-S_8 (Eldridge et al., 2021) and SO_4-H_2S (Eldridge et al., 2016) fractionation equations for each minerals pair, is valid. Note that isotopic composition of the sulfates is assumed to be constant because anhydrite is considered as an infinite reservoir.

FIGURE CAPTIONS

Fig. 1. Sampling locations on the simplified geological map of the Nappe des Gypses formation (Western French Alps; modified after Barré et al., 2020).

Figure 2: Typical sulfur-rich minerals observed in the Nappe des Gypses formation. (A) Pyrites in close association with anhydrite and white dolomite. (B, C) Crystals of elemental sulfur incorporated in gray dolomite “boudins” and diffuse elemental sulfur in the anhydrite facies. (D) Associated white dolomite, quartz, and pyrite association observed in carbonates-quartz-sulfides veins in micaschist layers. (E) Associated sulfides and elemental sulfur observed at the centimeter scale in the presence of micaschist at the Sollières l'Envers outcrop.

(F, G) Respective plane and cross-polarized light images depicting the typical occurrence of elemental sulfur in anhydrite. (H, I) Respective plane and cross-polarized light images depicting direct association of pyrites with white micas. Abbreviations: Anh = anhydrite; Py = pyrite; S = native sulfur; G-Dol = gray dolomite; W-Dol = white dolomite; Qtz = quartz; W-Mca = white micas; Fl = fluorite.

Fig. 3. $\delta^{34}S$ values of sulfates, sulfides, and elemental sulfur at each studied site. The gray shaded band shows $\delta^{34}S$ values typical of Carnian seawater (Claypool et al., 1980; Crockford et al., 2019). Error bars are smaller than the symbol sizes.

Fig. 4. $\Delta^{33}S$ vs. $\delta^{34}S$ diagrams for sulfates, sulfides, and elemental sulfur from each studied site. Outcrops are plotted from south to north: (A) Névache, (B) Bramans, (C) Ambin stream, (D) Sollières l'Envers, (E) Mont-Cenis Lake, and (F) Tignes. For each site, the mass fractionation exponent near 0.515 (i.e., for samples at isotopic equilibrium) between sulfates and elemental sulfur ($^{33}\theta_{SO_4\text{-}S_8}$) and between sulfates and sulfides ($^{33}\theta_{SO_4\text{-}H_2S}$) are calculated as well as the associated vector between sulfate and elemental sulfur (green arrow) and between sulfate and sulfide (red arrow). In these cases, isotopic equilibrium is confirmed (see section 5.4) and the associated equilibrium temperature is determined using the respective $\Delta^{34}S$ values and $SO_4\text{-}S_{8(aq)}$ (green; Eldridge et al., 2021) or $SO_4\text{-}H_2S_{(aq)}$ (red; Eldridge et al., 2016) fractionation equations. Two-component mixing curves (yellow dashed curves) are calculated between the most extreme sulfate and elemental sulfur compositions. In (A) and (B), the gray dashed curve is the mixing curve between sulfates and a theoretical organic sulfur reservoir (estimated at $\delta^{34}S = -30‰$ and the $\Delta^{33}S$ value determined using $^{33}\lambda = 0.5152$). Errors bars represent 1σ for dual-inlet mass-spectrometry measurements. Measurement errors on $\delta^{34}S$ are smaller than the symbol sizes.

Fig. 5. Plots of $^{33}\lambda$ vs. temperature between sulfates and either elemental sulfur (diamonds), pyrite (squares), or chalcopyrite (triangles). For each mineral pair, temperatures are estimated

from the respective $\Delta^{34}S$ values and SO_4-$S_{8(aq)}$ (Eldridge et al., 2021) or SO_4-$H_2S_{(aq)}$ (Eldridge et al., 2016) fractionation equations. Curves indicate the evolution of $^{33}\lambda$ as a function of temperature for different sulfur species relative to sulfates from theoretical calculations (CS_{2aq} is from Otake et al., 2008; H_2S_{aq} and SO_3^{2-} from Eldridge et al., 2016; S_8, S_3^- and S_n^{2-} from Eldridge et al., 2021). Errors represent 1σ for dual-inlet mass-spectrometry measurements.

Fig. 6. Elemental sulfur melting curve (black curve, shaded area indicates experimental errors; from Crapanzano, 2005). For comparison, the *P-T* path of the Nappe des Gypses formation (blue arrow and squares; Barré et al., 2020) and the elemental sulfur precipitation temperature determined herein (yellow shaded area; see section 5.4 for details) are shown. The Nappe des Gypses *P-T* path crosses the elemental sulfur melting curve at conditions consistent with the temperature range calculated from the isotopic compositions of our samples, indicating that all the elemental sulfur precipitated just after the D2-D3 tectonic transition during the exhumation of the Nappe des Gypses.

Fig. 7. $\Delta^{33}S$ vs. $\Delta^{36}S$ diagrams for sulfates, sulfides, and elemental sulfur from each studied site. Outcrops are plotted from south to north: (A) Névache, (B) Bramans, (C) Ambin stream, (D) Sollières l'Envers, (E) Mont-Cenis Lake, and (F) Tignes. Two-component mixing curves (yellow dashed curves) are calculated between the most extreme sulfate and elemental sulfur compositions. In (A) and (B), the gray dashed curve is the mixing curve between sulfates and a theoretical organic sulfur reservoir with estimated $\Delta^{33}S$ and $\Delta^{36}S$ values determined using $^{33}\lambda$ = 0.5152 and $^{36}\lambda$ = 1.89, respectively. The mass-dependent fractionation line (dashed black line of slope −6.9; Ono et al., 2006) is also shown for comparison. Errors bars represent 1σ for dual-inlet mass-spectrometry measurements.

Fig. 8. Schematic summary of the TSR reaction pathway and associated isotopic fractionations. (Left) The initial thermodynamic state (Truche et al., 2014), isotopic signatures (this study), and relative proportions (Barré et al., 2017) of sulfates and elemental sulfur

reservoirs in the fluid during TSR. (Right) Three possibilities for generating the observed elemental sulfur and sulfide compositions. (1) When no metal is present in the system, the combination of polysulfides leads to elemental sulfur precipitation at isotopic equilibrium with the sulfate; the resulting isotopic signature is temperature dependent. (2) When a large amount of metal is released into the system, all reduced sulfur species (H_2S and S_n^{2-}) precipitate as sulfide at isotopic equilibrium with sulfate and experience a temperature-dependent isotopic fractionation. (3) When only a small amount of metal (i.e., less than the reduced sulfur species) is released into the system, only some of the H_2S precipitates as sulfide. The resulting disequilibrium isotopic composition of the sulfides corresponds to the mixing between 33% elemental sulfur (i.e., polysulfides) with 67% sulfate. The similarity of the calculated and measured sulfide isotopic compositions (bottom right) confirms that the disequilibrium sulfides precipitated from the mixing of sulfates and polysulfides.

754 Figure 1

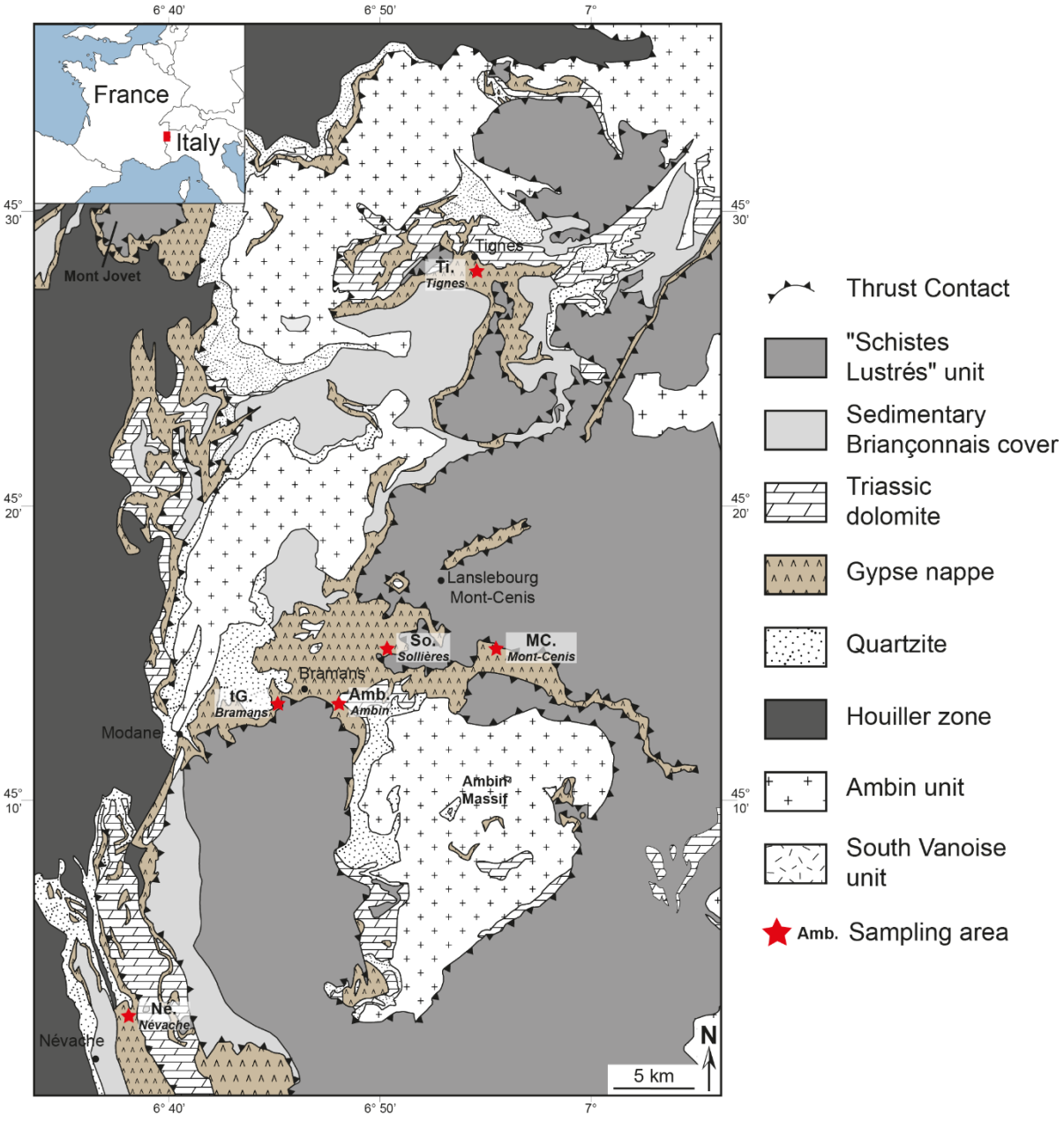

755

756

Figure 2

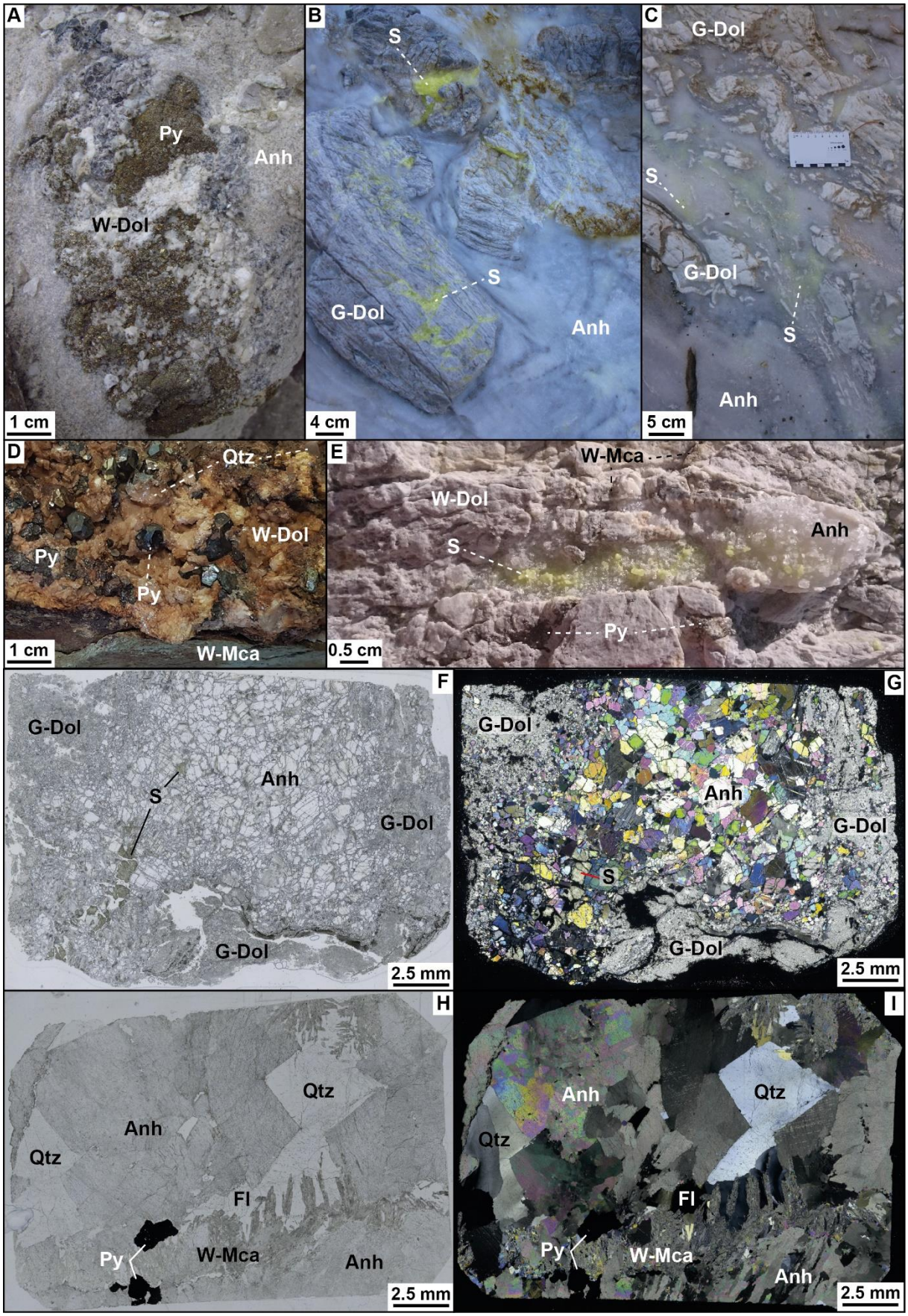
A
Py
Anh
W-Dol
1 cm
B
S
S
G-Dol
Anh
4 cm
C
G-Dol
S
G-Dol
S
Anh
5 cm
D
Qtz
W-Dol
Py
Py
1 cm
W-Mca
E
W-Mca
W-Dol
Anh
S
Py
0.5 cm
F
G-Dol
Anh
S
G-Dol
G-Dol
2.5 mm
G
G-Dol
Anh
G-Dol
S
G-Dol
2.5 mm
H
Qtz
Anh
Qtz
Fl
Py
W-Mca
Anh
2.5 mm
I
Anh
Qtz
Qtz
Fl
Py
W-Mca
Anh
2.5 mm

759 Figure 3

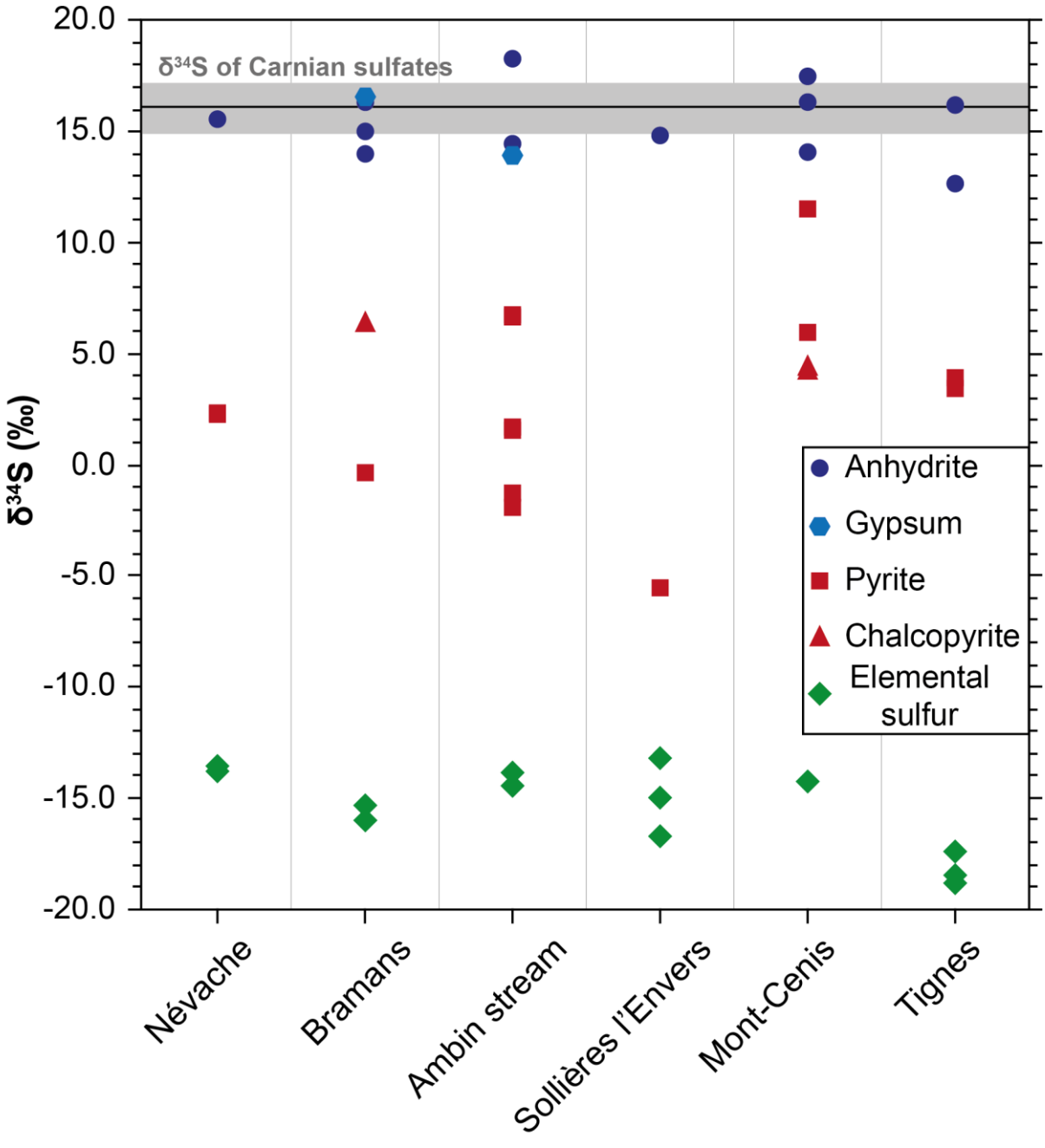

760

761

762 Figure 4

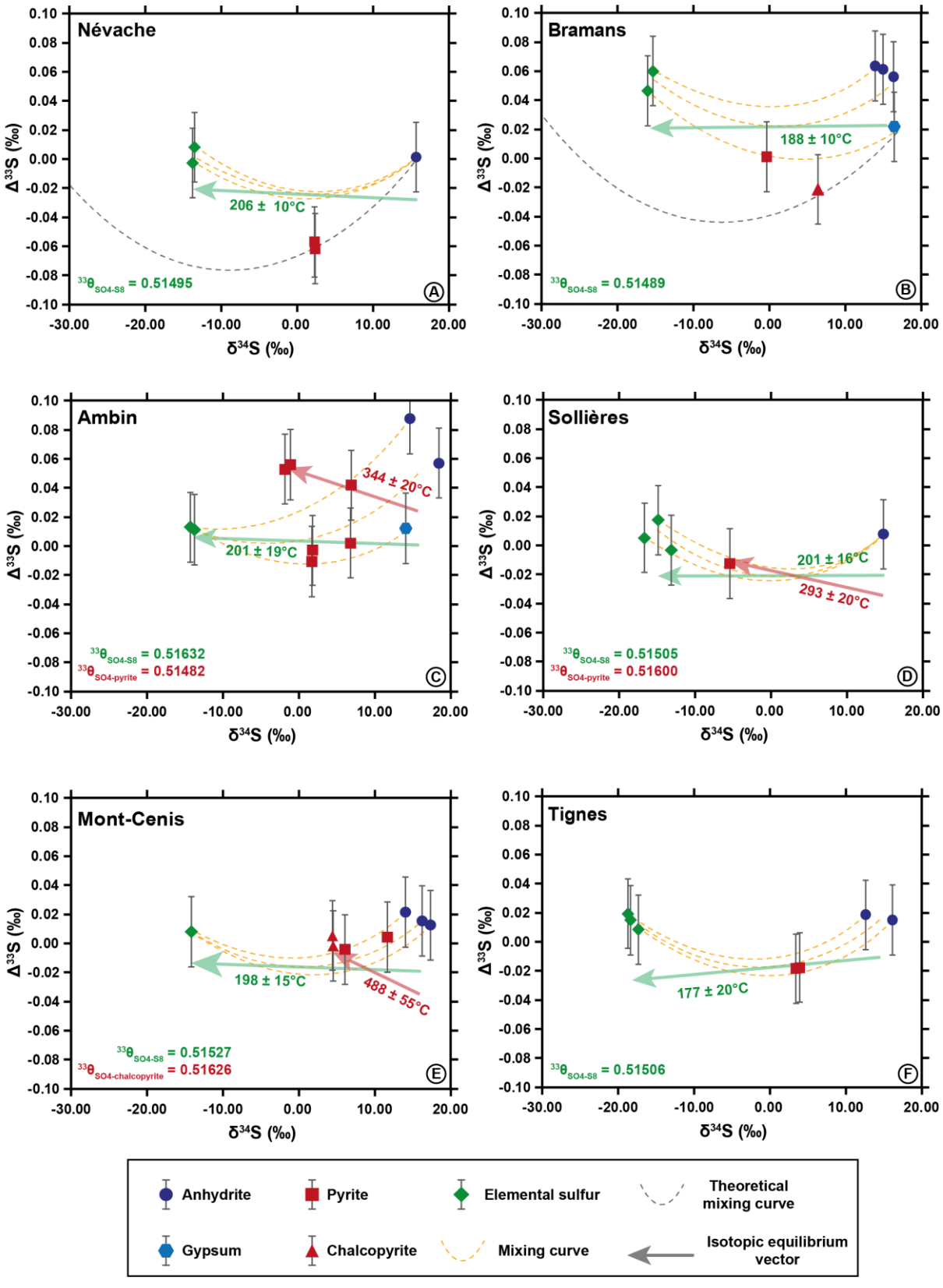

763

764

765 Figure 5

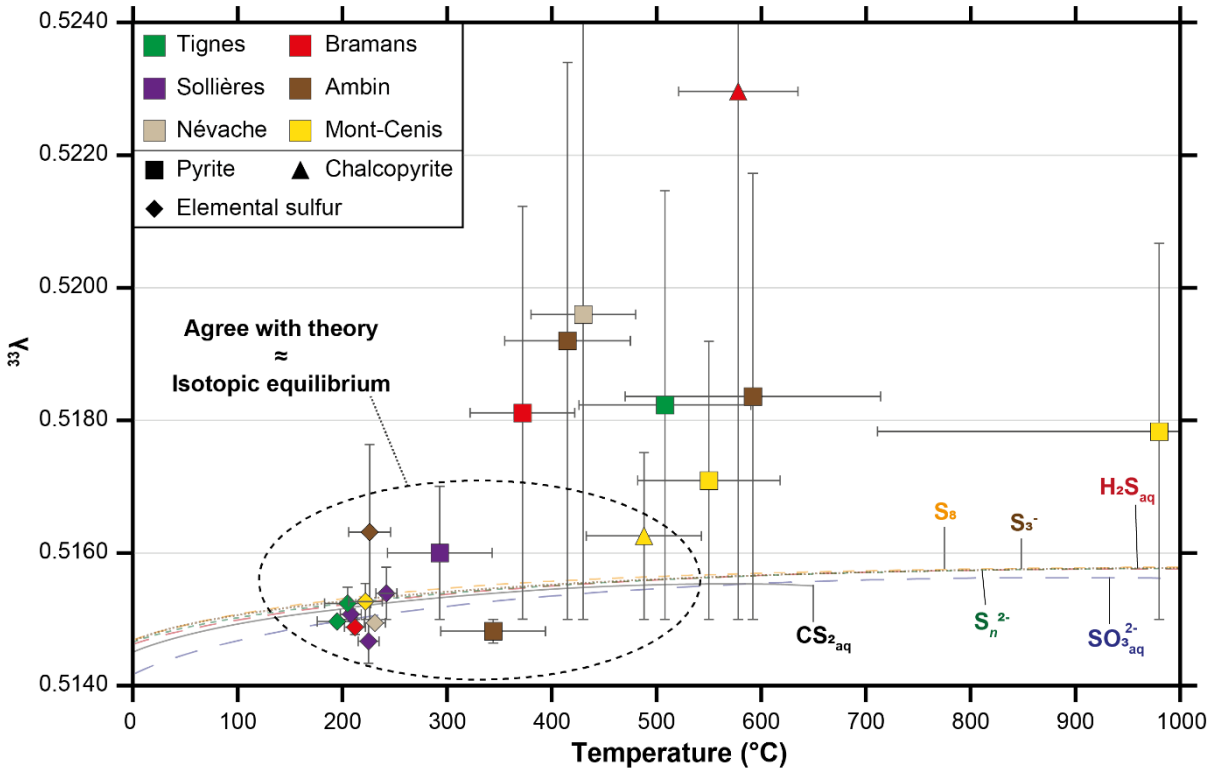

766

767

768 Figure 6

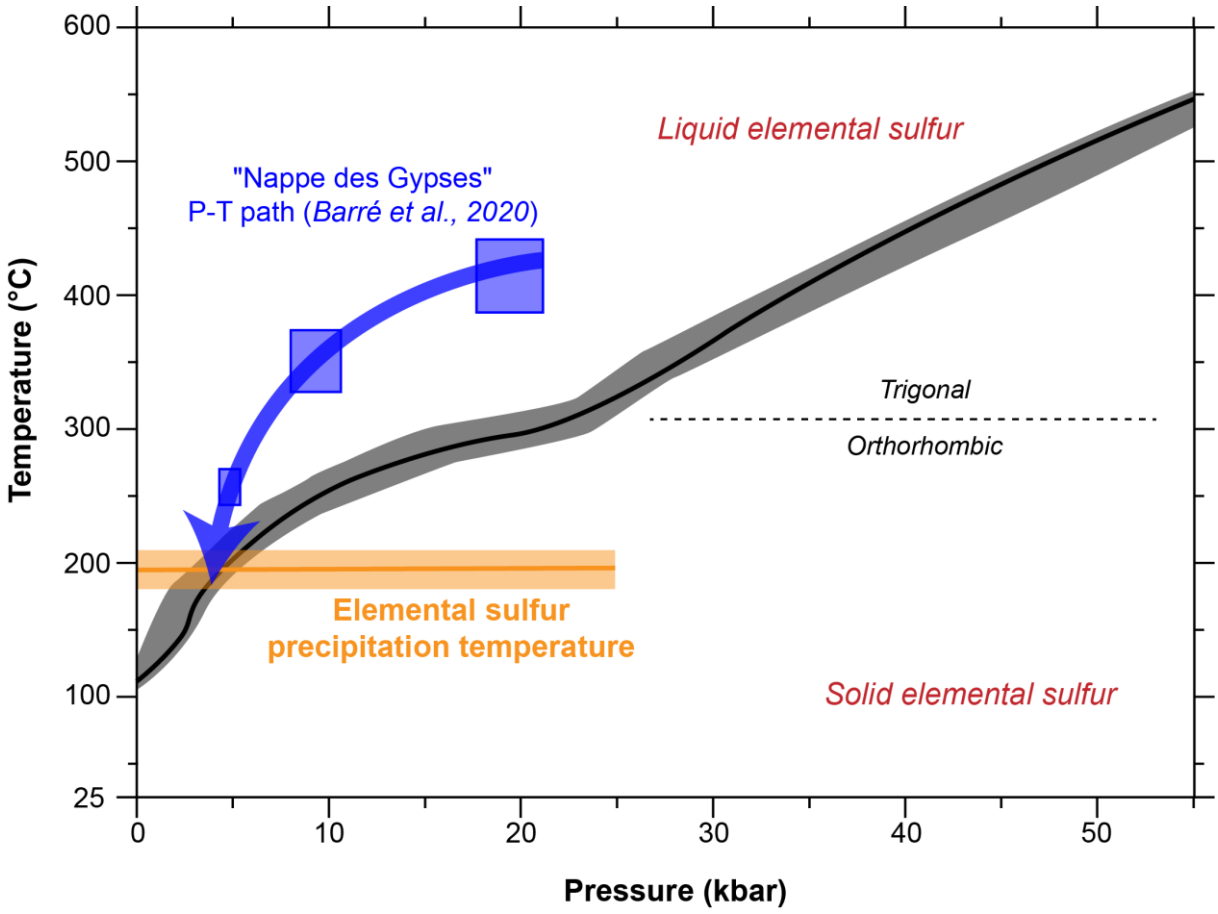

769

770

771 Figure 7

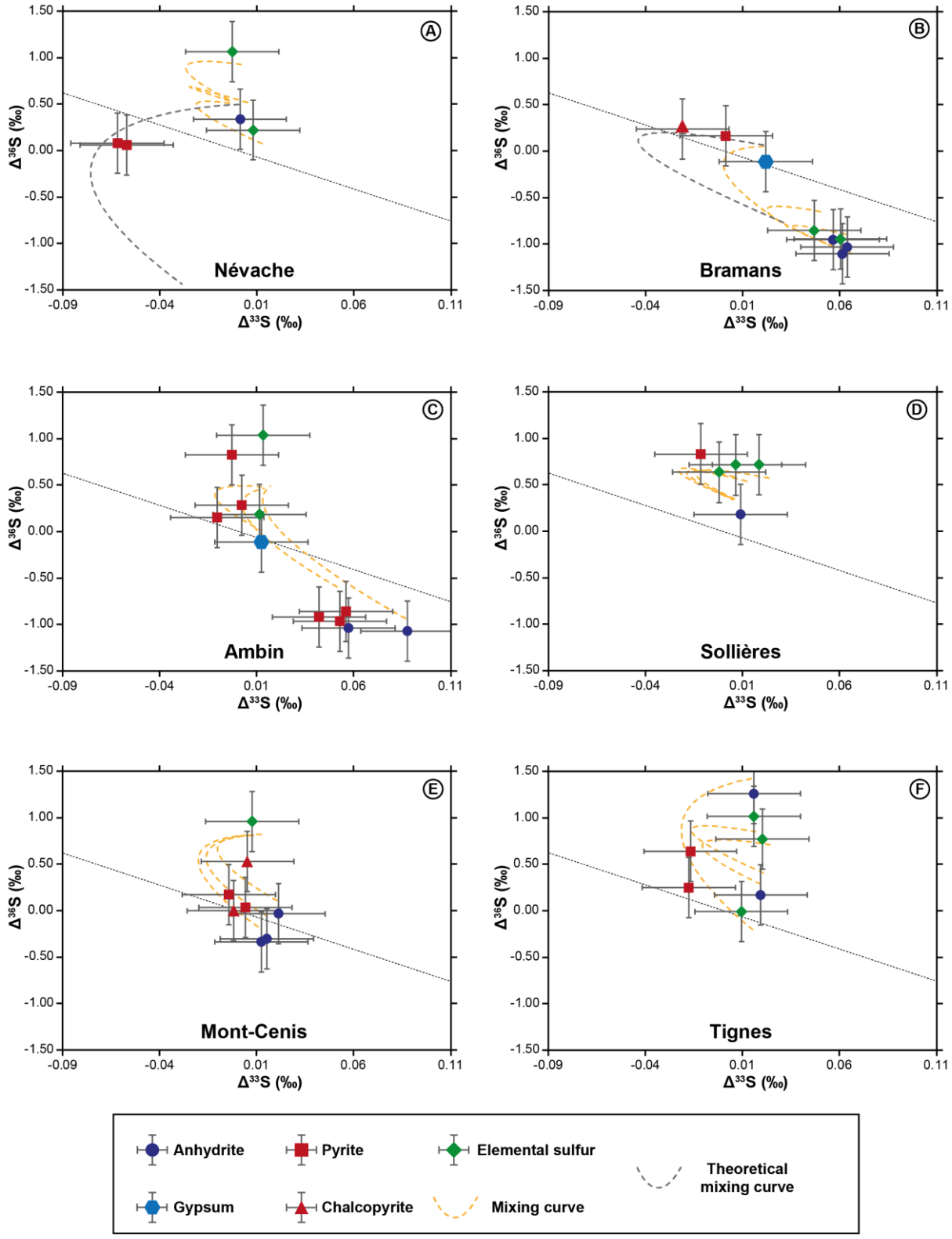

772

773

774 Figure 8

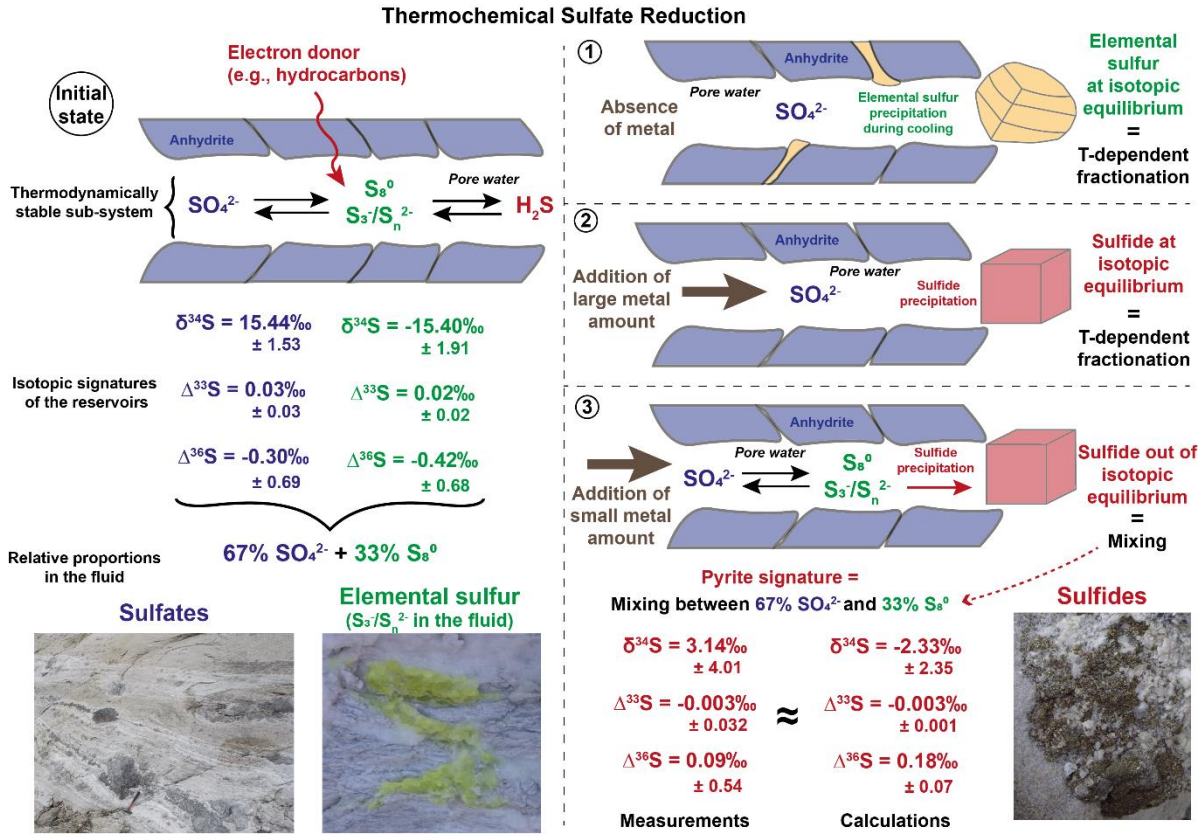

775

776

777 Table 1

Sample	Mineral	$\delta^{33}S$ (‰)	± σ	$\delta^{34}S$ (‰)	± σ	$\delta^{36}S$ (‰)	± σ	$\Delta^{33}S$ (‰)	$\Delta^{36}S$ (‰)
Névache									
Né.1.2	Anhydrite	8.02	0.012	15.64	0.007	30.26	0.030	0.00	0.34
Né.3.1	Pyrite	1.15	0.008	2.34	0.006	4.52	0.092	-0.06	0.06
Né.3.2	Pyrite	1.15	0.010	2.36	0.005	4.56	0.083	-0.06	0.08
Né.S8.1	Elemental sulfur	-7.09	0.013	-13.71	0.008	-24.82	0.255	0.00	1.06
Né.S8.2	Elemental sulfur	-6.97	0.008	-13.51	0.006	-25.29	0.070	0.01	0.22
Bramans									
tG.1.1	Anhydrite	8.49	0.019	16.43	0.035	30.50	0.115	0.06	-0.95
tG.1.2	Anhydrite	7.80	0.014	15.08	0.011	27.74	0.091	0.06	-1.11
tG.11	Anhydrite	7.29	0.012	14.07	0.012	25.88	0.075	0.06	-1.04
tG.16.1	Gypsum	8.52	0.006	16.57	0.012	31.60	0.162	0.02	-0.11
tG.12.1	Pyrite	-0.15	0.009	-0.30	0.002	-0.41	0.128	0.00	0.16
tG.16.S2	Chalcopyrite	3.31	0.013	6.47	0.006	12.57	0.132	-0.02	0.23
tG.S0.1	Elemental sulfur	-8.22	0.011	-16.00	0.009	-31.03	0.111	0.05	-0.85
tG.S0.2	Elemental sulfur	-7.83	0.013	-15.26	0.004	-29.74	0.030	0.06	-0.95
Ambin									
Amb.4.SO.1	Anhydrite	7.54	0.036	14.52	0.041	26.70	0.178	0.09	-1.07
Amb.4.SO.2	Anhydrite	9.49	0.012	18.39	0.011	34.19	0.064	0.06	-1.04
Amb.1	Gypsum	7.19	0.014	13.99	0.004	26.63	0.084	0.01	-0.11
Amb.4.S2.1	Pyrite	-0.91	0.006	-1.88	0.006	-4.53	0.092	0.05	-0.97
Amb.4.S2.2	Pyrite	-0.55	0.015	-1.18	0.022	-3.10	0.098	0.06	-0.86
Amb.2.1	Pyrite	3.56	0.017	6.84	0.017	12.12	0.105	0.04	-0.92
Amb.2.2	Pyrite	3.48	0.009	6.77	0.002	13.17	0.089	0.00	0.28
Amb.B.S.1	Pyrite	0.91	0.009	1.77	0.006	4.18	0.358	0.00	0.82
Amb.B.S.2	Pyrite	0.82	0.005	1.62	0.003	3.23	0.066	-0.01	0.15
Amb.3.1	Elemental sulfur	-7.40	0.007	-14.34	0.007	-26.03	0.324	0.01	1.03
Amb.3.2	Elemental sulfur	-7.10	0.010	-13.77	0.005	-25.82	0.133	0.01	0.18
Sollières									
αSo.3	Anhydrite	7.66	0.006	14.91	0.008	28.70	0.217	0.01	0.18
αSo.2.2	Pyrite	-2.82	0.008	-5.44	0.011	-9.49	0.273	-0.01	0.82
So.D.1.S8	Elemental sulfur	-8.64	0.006	-16.72	0.005	-30.82	0.217	0.01	0.71
αSo.2.3	Elemental sulfur	-6.80	0.011	-13.17	0.003	-24.24	0.191	0.00	0.63
So.4	Elemental sulfur	-7.68	0.010	-14.90	0.002	-27.42	0.204	0.02	0.71
Mont-Cenis									
MC.4.SO.1	Anhydrite	7.21	0.011	14.00	0.004	26.74	0.111	0.02	-0.03
MC.4.SO.2	Anhydrite	8.88	0.011	17.28	0.005	32.76	0.074	0.01	-0.33
MC.2	Anhydrite	8.33	0.008	16.20	0.008	30.71	0.122	0.02	-0.30
MC.3.1.1	Pyrite	3.10	0.005	6.04	0.006	11.68	0.076	0.00	0.17
MC.3.1.4	Pyrite	5.96	0.005	11.60	0.004	22.20	0.050	0.00	0.04
MC.3.1.2	Chalcopyrite	2.29	0.007	4.45	0.004	8.47	0.111	0.00	0.00
MC.3.1.3	Chalcopyrite	2.24	0.012	4.34	0.005	8.79	0.192	0.01	0.53
MC.4.S8	Elemental sulfur	-7.36	0.010	-14.25	0.004	-25.95	0.220	0.01	0.96
Tignes									
Ti.1.SO	Anhydrite	8.36	0.007	16.27	0.006	32.40	0.093	0.02	1.26
Ti.2.SO	Anhydrite	6.56	0.015	12.74	0.006	24.52	0.052	0.02	0.17
Ti.3.1	Pyrite	2.06	0.007	4.03	0.010	8.31	0.171	-0.02	0.64
Ti.3.2	Pyrite	1.77	0.010	3.48	0.008	6.87	0.081	-0.02	0.25
Ti.1.S8.1	Elemental sulfur	-9.52	0.009	-18.43	0.006	-33.71	0.230	0.02	1.01
Ti.1.S8.2	Elemental sulfur	-9.72	0.005	-18.82	0.004	-34.69	0.175	0.02	0.77
Ti.2.S8	Elemental sulfur	-8.98	0.011	-17.39	0.005	-32.79	0.123	0.01	-0.01

778

779 Table 2

Locality	Sample	Mineral	$^{33}\lambda$	1σ	$^{36}\lambda$	1σ	T°C	1σ	Valid temperature?
Névache	Né.3	Pyrite	0.51960	0.00460	1.91973	0.02973	430	20	No
	Né.S8	Elemental sulfur	0.51495	0.00005	1.88873	0.00134	206	10	Yes
Bramans	tG.12.1	Pyrite	0.51812	0.00311	1.84051	0.04949	372	20	No
	tG.16.S2	Chalcopyrite	0.52296	0.00796	1.78740	0.10260	578	57	No
	tG.S0	Elemental sulfur	0.51489	0.00012	1.90484	0.01484	188	10	Yes
Ambin	Amb.4.S2	Pyrite	0.51482	0.00018	1.91167	0.02167	344	20	Yes
	Amb.2	Pyrite	0.51836	0.00336	1.85402	0.03599	592	122	No
	Amb.B.S	Pyrite	0.51920	0.00420	1.81325	0.07675	415	60	No
	Amb.3	Elemental sulfur	0.51632	0.00132	1.85488	0.03512	201	19	Yes
Sollières	αSo.2.2	Pyrite	0.51600	0.00100	1.86761	0.02239	293	20	Yes
	So.D.1.S8	Elemental sulfur	0.51508	0.00008	1.88250	0.00751	185	10	Yes
	αSo.2.3	Elemental sulfur	0.51539	0.00039	1.88320	0.00682	217	10	Yes
	So.4	Elemental sulfur	0.51467	0.00033	1.88139	0.00862	200	10	Yes
Mont-Cenis	MC.3.1.1	Pyrite	0.51710	0.00210	1.86016	0.02984	550	68	No
	MC.3.1.4	Pyrite	0.51783	0.00283	1.84000	0.05000	980	269	No
	MC.3.2	Chalcopyrite	0.51626	0.00126	1.85803	0.03197	488	55	Yes
	MC.4.S8	Elemental sulfur	0.51527	0.00027	1.86009	0.02991	198	15	Yes
Tignes	Ti.3	Pyrite	0.51823	0.00323	1.92388	0.03388	508	82	No
	Ti.1.S8	Elemental sulfur	0.51497	0.00004	1.89314	0.00317	172	18	Yes
	Ti.2.S8	Elemental sulfur	0.51524	0.00024	1.92214	0.03215	182	21	Yes

780